Zahn, R., Comas, M.C., and Klaus, A. (Eds.), 1999
Proceedings of the Ocean Drilling Program, Scientific Results, Vol. 161

27. EVIDENCE FOR MIOCENE SUBDUCTION BENEATH THE ALBORAN SEA: $^{40}AR/^{39}AR$ DATING AND GEOCHEMISTRY OF VOLCANIC ROCKS FROM HOLES 977A AND 978A[1]

Kaj Hoernle,[2] Paul van den Bogaard,[2] Svend Duggen,[2] Beate Mocek,[2] and Dieter Garbe-Schönberg[3]

ABSTRACT

Volcanic pebbles in gravels from Sites 977 and 978 in the Alboran Sea (western Mediterranean) were dated (using the $^{40}Ar/^{39}Ar$ single-crystal laser technique) and analyzed for their major- and trace-element compositions (determined by X-ray fluorescence and inductively coupled plasma-mass spectrometry). The samples range from basalts to rhyolites, and belong to the tholeiitic, calc-alkaline, and shoshonitic series. Single-crystal and step-heating laser $^{40}Ar/^{39}Ar$ analyses of plagioclase, sanidine, biotite, and amphibole phenocrysts from basaltic to rhyolitic samples indicate that eruptions occurred between 6.1 and 12.1 Ma. The age data conform to the stratigraphy and agree with microfossil ages, when available. The major-element and compatible trace-element data of samples with $H_2O < 4$ wt% show systematic variations, consistent with fractionation of the observed phenocryst phases (plagioclase, olivine, clinopyroxene, magnetite, hornblende, quartz, and biotite). The incompatible-element patterns formed by normalizing to primitive mantle for all samples show spiked patterns with peaks generally at mobile elements and troughs at immobile elements, in particular Nb and Ta. The calc-alkaline affinities and the incompatible-element systematics are characteristic of subduction zone volcanism, which indicates that subduction occurred beneath the eastern Alboran from 6 to at least 12 Ma. We propose that the change in chemistry from calc-alkaline and potassic to sodic compositions between 5–6 Ma reflects detachment of the subducting slab. Uplift of the Strait of Gibraltar, associated with this detachment, could have caused the Messinian Salinity Crises.

INTRODUCTION

Neogene volcanic rocks extend from southeastern Spain through the eastern Alboran Sea to northeastern Morocco and northwestern Algeria, and form a north-northeast–trending belt, ~400 km long and ~200 km wide (Fig. 1; Le Pichon et al., 1972; Horvarth and Berckhemer, 1982; Zeck, 1996). Based on K/Ar age determination of whole-rock samples, calc-alkaline volcanic rocks in southeast Spain and northern Africa range in age from ~5 to 18 Ma (Fig. 2; Bellon and Brousse, 1977; Bellon et al., 1983; Hernandez and Bellon, 1985; Nobel et al., 1981; Fernandez Soler, 1992). Basalt dike swarms, outcropping over large areas of the western Betics, extend the age of magmatism in southern Spain to 23 Ma (Torres-Roldán et al., 1986). Volcanic rocks with calc-alkaline and tholeiitic affinities also occur on Alboran Island (7–25? Ma; Aparicio et al., 1991; Bellon and Letouzey, 1977). Although the acoustic basement beneath the eastern and southern Alboran Sea is considered to consist mainly of volcanic rocks (Comas et al., 1992) and volcanic rocks were sampled by dredging or submersibles (Giermann et al., 1968; Comas, Zahn, Klaus, et al., 1996; Hoernle et al., 1997), no published data are available for the age and composition of these volcanic rocks. Volumetrically insignificant amounts of ultrapotassic rocks and alkali basalts are present in the upper Miocene (Messinian) and Pliocene, respectively, in the Alboran Region.

A long-standing paradox has been how to explain the formation of the western Mediterranean through extension, rifting, and seafloor spreading at the same time (Eocene–Miocene) that the African and European Plates were colliding (Dewey et al., 1989). The formation of Mediterranean-type back-arc basins (Horvarth and Berckhemer, 1982), as exemplified by the Alboran Basin, reflects this paradox in miniature. The many models that have been proposed to explain the origin of the Alboran can be divided into three general groups. The first group calls upon mantle diapirism beneath the Alboran to uplift the lithosphere and form the nappe structures in the Betic-Rif mountains and the Gibraltar arc (Loomis, 1975; Weijermars, 1985). The second group proposes removal and detachment of thickened lithospheric mantle by either delamination or convection (e.g., Platt and Vissers, 1989; García-Dueñas et al., 1992; Morley 1992, 1993; Comas et al., 1992; Docherty and Banda, 1995; Vissers et al., 1995; Seber et al., 1996a, 1996b). The third group relates the Alboran Basin formation to subduction (e.g., Araña and Vegas, 1974; Torres-Roldán et al., 1986; Dercourt et al., 1986; DeJong, 1993; Zeck et al., 1992; Blanco and Spakman, 1993; Royden, 1993; Zeck, 1996). Each of the three groups of models will be associated with volcanism having distinct chemical characteristics. Therefore, studies of volcanic rocks from this region, combined with the results of geophysical, structural, and tectonic studies, can help improve our understanding of the geodynamic evolution of the Alboran Region.

In this study, we present age data obtained using the $^{40}Ar/^{39}Ar$ single-crystal laser technique, and major- and trace-element compositions of 24 volcanic pebbles (classified as such on the basis of their size) from Ocean Drilling Program Holes 977A and 978A in the Alboran Sea (Fig. 3; Comas, Zahn, Klaus, et al., 1996). The pebbles range from rounded to angular in shape and from basalt to rhyolite in composition. They occur in gravel (or conglomerate) layers of late Messinian (Site 978) and Miocene (Site 977) age, which are interpreted to reflect channel fill. Based on the morphology of the northern, central Alboran Basin, the pebbles are likely to be derived from both local (Yusuf Ridge, Al-Mansour Seamount) and more distal sources (Alboran Ridge, Cabo de Gata; Comas, Zahn, Klaus, et al., 1996), and thus provide us with a representative sampling of this region. We use the pebbles to place constraints on the origin of volcanism in the central portion of the north-northeast–trending belt of Miocene volcanism in the Alboran Region (Fig. 1).

PETROGRAPHY

The thin-section petrography of the volcanic clasts from Holes 977A and 978A is summarized in Table 1 for all samples except 7647-O (161-978A-47R-1, 0–6 cm), 7519-II (161-978A-47R-1, 4–9

[1]Zahn, R., Comas, M.C., and Klaus, A. (Eds.), 1999. *Proc. ODP, Sci. Results,* 161: College Station, TX (Ocean Drilling Program).
[2]GEOMAR Research Center, Wischhofstrasse 1-3, 24148 Kiel, Federal Republic of Germany. khoernle@geomar.de
[3]Christian Albrechts Universität zu Kiel, Olshausenstrasse 40, 24118 Kiel, Federal Republic of Germany.

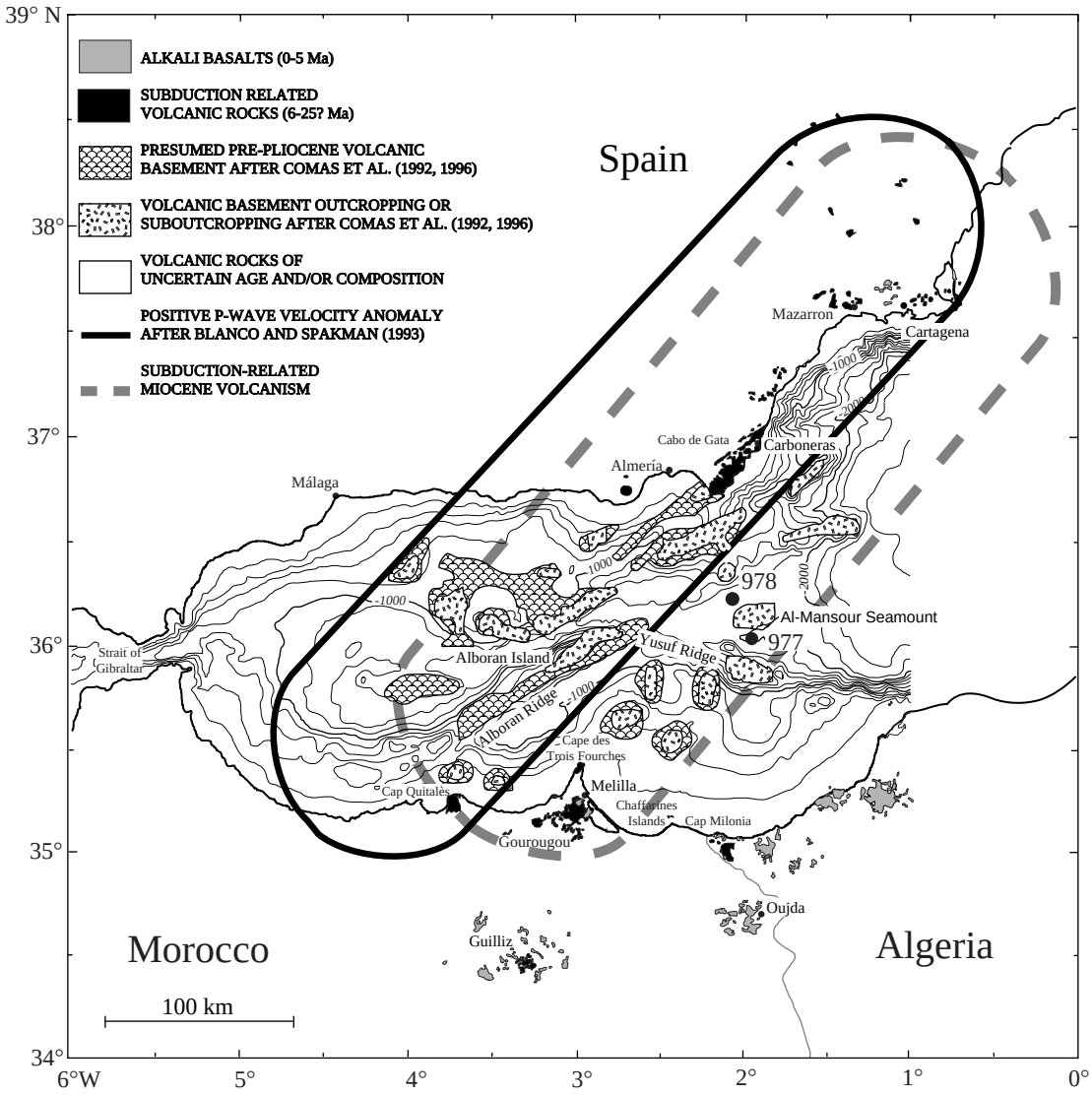

Figure 1. Map of the Alboran Sea and surrounding regions. The region containing Miocene subduction-related (calc-alkaline and ultrapotassic) volcanic rocks (encircled with a dashed line) correlates well with the outline (solid line) of the central portion of the synthetic slab SYN1 at 247 km depth from the *P*-wave seismic tomographic results of Blanco and Spakman (1993). Data come from the following sources: Ait-Brahim and Chotin (1990), Araña and Vegas (1974), Bellon (1976), Bellon and Brousse (1977), Bellon et al. (1983), Blanco and Spakman (1993), Bordet et al., (1982), Bourdier (1986), Comas et al. (1992), M. Comas (pers. comm., 1995), Di Battistini et al. (1987), Dupuy et al., (1986), Fernandez Soler (1992), Hernandez and Bellon (1985), Hernandez et al., (1987), Munksgaard (1984), Torres-Roldán et al. (1986), Venturelli et al. (1984), and Zeck (1996).

cm), and 7647-B (978A-47R-1, 0–6 cm), for which sufficient material was not available.

The basalts through rhyolites contain ≤35% phenocrysts, although most have <25%. Plagioclase is the most abundant phenocryst phase in all rock types (Fig. 4). In basaltic rocks (basalts and basaltic andesites), the abundance of plagioclase ranges from 5% to 15%, with the exception of basaltic andesite sample 7519 (161-978A-46R-1, 4–9 cm), which contains 30%. Oscillatory zoning occurs in some plagioclase phenocrysts. The other phenocryst phases include clinopyroxene (≤8%), magnetite (≤2%), amphibole (≤2%), and olivine (≤1%), with most phenocrysts being subhedral. The groundmass contains the same phases as are present as phenocrysts. Secondary phases in some of the samples include chlorite, epidote, hematite, magnetite, ilmenite, pyrite, biotite, and calcite. Breakdown to secondary chlorite or epidote can affect clinopyroxene and plagioclase phenocrysts and the groundmass. Sample 7520 (161-977A-60X-1, 27–31 cm) contains 10% quartz as veins and vesicle filling.

The andesite samples contain phenocrysts of plagioclase (10%–20%), clinopyroxene (≤5%), orthopyroxene (≤5%), and magnetite (≤1%). With the exception of some anhedral clinopyroxene, all phenocrysts are subhedral. The groundmass consists primarily of plagioclase, with some orthopyroxene. Secondary phases include Na-rich feldspar, chlorite, epidote, calcite, magnetite, and pyrite. Sample 7649 (161-977A-62X-1, 4–9 cm) has 5% quartz as vesicle fill. Secondary chlorite, epidote and/or calcite results from partial breakdown of plagioclase and clinopyroxene.

Phenocrysts in the dacites and rhyolites include plagioclase (5%–20%), quartz (≤10%), orthopyroxene (≤5%), clinopyroxene (≤2%), amphibole (≤3%), biotite (≤3%), magnetite (≤2%), and sanidine (≤1%). Plagioclase phenocrysts range from euhedral to subhedral, whereas other phenocryst phases range from subhedral to anhedral. Secondary phases include epidote, chlorite, actinolite, titanite, chlorite, magnetite, and calcite. Rounded grains of quartz in some of these samples are interpreted to be xenocrysts. The partial replacement of

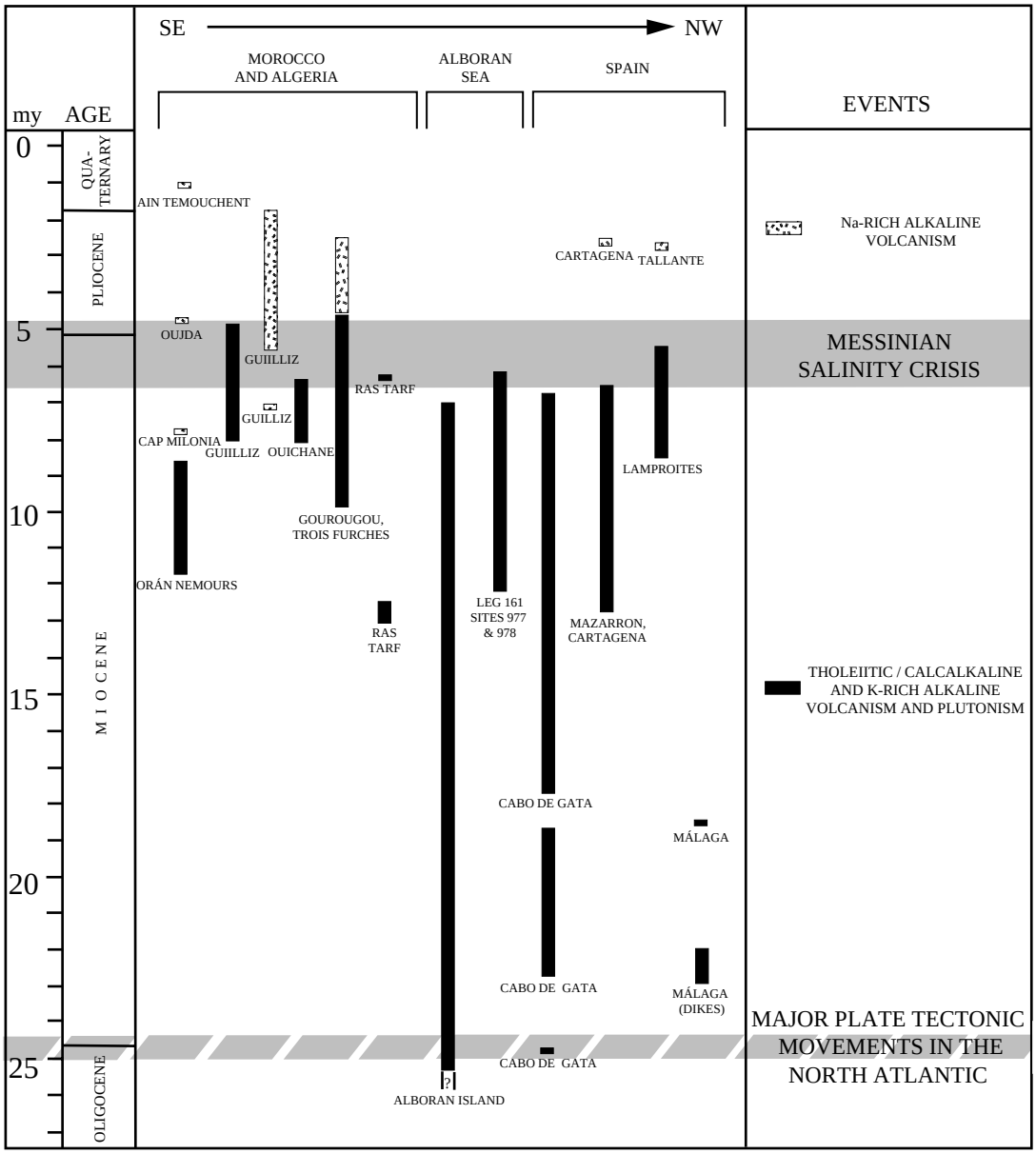

Figure 2. Diagram summarizes the magmatic history of the Alboran Region. Subduction-related volcanism and plutonism (tholeiitic, calc-alkaline, and K-rich) occurred from ~25 Ma to ~5–6 Ma. In the Messinian, the composition of the volcanic rocks changed to Na-rich, alkaline compositions. Data sources are the same as in Figure 1 and also include Harland et al. (1982) and Kastens (1992).

pyroxene, plagioclase, amphibole, and biotite by secondary chlorite, epidote, and actinolite is common.

Sample 7646 (161-977A-62X-1, 9–13 cm) is a coarse-grained granite, whereas Samples 7647-H (978A-47R-1, 0–6 cm), 7647-I (978A-47R-1, 0–6 cm), and 7647-U (978A-47R-1, 0–6 cm) have metamorphic textures, although their chemistries are consistent with a volcanic origin (see below).

Additional petrographic data from volcanic pebbles from Sites 977 and 978 were also reported by the Shipboard Scientific Party (Comas, Zahn, Klaus, et al., 1996).

ANALYTICAL METHODS

Age determinations by laser $^{40}Ar/^{39}Ar$ analysis were performed on single crystals of plagioclase, amphibole, and biotite, which were handpicked from crushed and sieved splits of Samples 161-977A-60X-1, 0–7 cm, 61X-1, 0–7 cm, 62X-1, 13–19 cm, and 978A-47R-1, 0–6 cm. Mineral separates were etched in 15% hydrofluoric acid (plagioclase and amphibole) and cleaned using an ultrasonic disintegrator (all separates). Samples were irradiated for 72 hours at a neutron current of 2.1×10^{12} N/cm^2 at the 5-MW reactor of the GKSS Research Center (Geesthacht, Federal Republic of Germany), with crystals in aluminum trays and irradiation cans wrapped in 0.7-mm cadmium foil.

Analyses of $^{40}Ar/^{39}Ar$ were conducted at the Geomar Tephrochronology Laboratory. Plagioclase and amphibole crystals were fused in a single step, whereas analyses of biotite were performed by laser step-heating (40 mW–2000 mW). Purified gas samples were analyzed using a MAP 216 series noble gas mass spectrometer. Raw mass spectrometer peaks were corrected for mass discrimination, background, and blank values (determined every fifth analysis). The

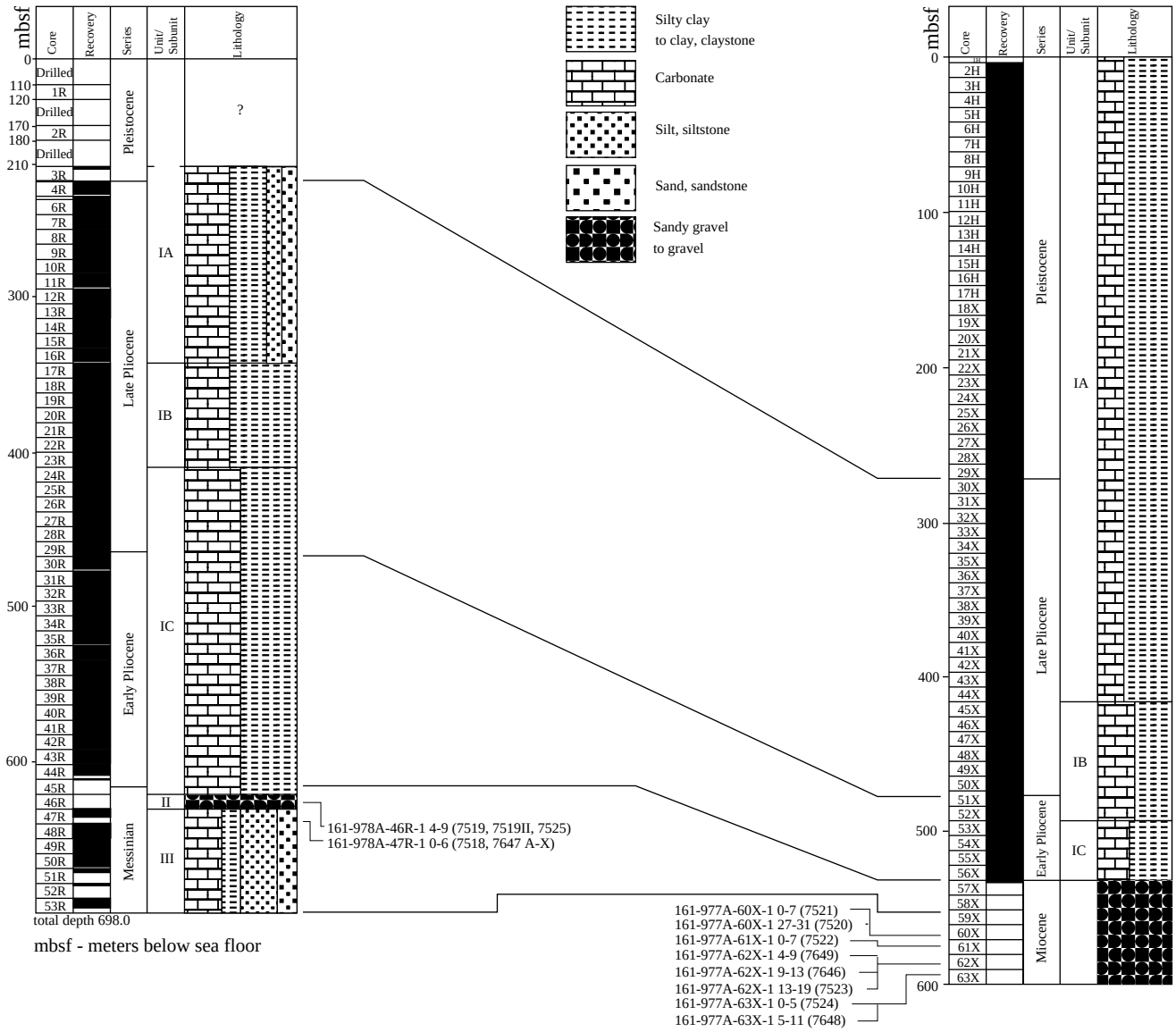

Figure 3. Stratigraphic sections from Holes 977A and 978A (Comas, Zahn, Klaus, et al., 1996) show the location of samples evaluated in this study.

neutron flux was monitored using TCR sanidine (Taylor Creek Rhyolite, 27.92 Ma; Dalrymple and Duffield, 1988; Duffield and Dalrymple, 1990) and internal standard SAN6165 (0.470 Ma; van den Bogaard, 1995). Vertical variations in J-values were quantified by a cosine function fit. Lateral variations in J were not detected. Corrections for interfering neutron reactions on Ca and K are based on analyses of optical grade CaF_2 and high-purity K_2SO_4 salt crystals that were irradiated together with the samples. Correction factors were determined as $^{36}Ar/^{39}ArCa = 0.465 \pm 0.001$; $^{37}Ar/^{39}ArCa = 977 \pm 2$; $^{38}Ar/^{39}ArK = 0.0222 \pm 0.0001$; and $^{40}Ar/^{39}ArK = 0.002 \pm 0.001$. Analytical errors are quoted as 1σ.

For major- and trace-element analyses, the volcanic pebbles were cleaned, crushed to 0.5 cm size, handpicked, and then washed with distilled water. Whole-rock chips were ground to rock powder in an agate mill. Both H_2O and CO_2 contents were determined using a Rosemount Infrared Photometer CSA 5003. Bulk-rock analyses of major and trace elements (Ba, Rb, Sr, Zr, V, Cr, Co, Ni, Cu, Zn, and Ga) were performed on fused tablets. The tablets were analyzed at the GEOMAR Research Center using a Philips X′ unique PW 1480 X-ray fluorescence spectrometer. International reference standards RGM-1 (rhyolite), BM (basalt), SY-2 (syenite), and SDC-1 (mica schist) were also analyzed and are used to evaluate the precision and accuracy of the measurements (Table 2). The maximum standard deviation of the standards is 0.20 wt% for SiO_2 and 0.02 wt% for all other major elements except Na_2O (0.10 wt%). For the trace elements measured by XRF, the maximum standard deviation is 5 ppm, with the exception of Ba, for which it is 14 ppm.

Additional trace elements (Pb, Th, U, Hf, Nb, Ta, Y, and all rare earth elements [REE]) were analyzed using an upgraded VG Plasmaquad PQ1 ICP-MS at the Geological Institute, University of Kiel, after the method of Garbe-Schoenberg (1993). Two blanks and international standards BHVO-1 (basalt), RGM-1 (rhyolite), and STM-1 (syenite) were analyzed with the samples. Results are presented in Table 3. Precision of the results was estimated from duplicate digestions and duplicate measurements and was found to be <2%–5% relative standard deviation in most cases.

AGE DETERMINATIONS

To determine the eruption ages of submarine lava clasts drilled at Sites 977 and 978, laser $^{40}Ar/^{39}Ar$ age determinations were performed

Table 1. Thin-section petrography.

Sample no.	Rock type	Core, section, interval (cm)	Ol	Cpx	Opx	Plg	Amph	Bio	Alk. fsp	Qtz	Mt	Pyr	Cc	Act	Groundmass	Alteration
7518	Basalt	161-978A-47R-1, 0-6	1	2	—	—	15	—	—	—	2	—	—	—	Ol, px, plg, mt, chl	Heavy
7647-Q	Basalt	978A-47R-1, 0-6	—	—	—	10	—	—	—	—	—	—	—	—	Px, plg, mt	Slight
7523	Basalt	977A-62X-1, 13-19	1	10	—	10	2	—	—	—	1	—	—	—	Px, plg, mt, ep	Slight
7519	Bas. andesite	978A-46R-1, 4-9	—	3	—	30	—	—	—	—	1	—	1	—	Variolites, mt, ep	Slight
7520	Bas. andesite	977A-60X-1, 27-31	—	7	—	5	—	—	—	10	—	5	—	—	Px, fsp, chl, ep	Heavy
7647-K	Andesite	978A-47R-1, 0-6	—	5	—	20	—	—	—	—	1	—	1	—	Plg, mt, chl, ep	Heavy
7649	Andesite	977A-62X-1, 4-9	—	<1	5	10	—	—	—	5	—	2	—	—	Opx, plg, chl, ep, pyr	Heavy
7524	Dacite	977A-63X-1, 0-5	—	2	—	10	—	—	—	5	2	—	—	8	Px, plg, qtz, mt, act, chl	Moderate
7525	Dacite	978A-46R-1, 4-9	—	—	5	20	—	2	—	1	2	—	—	—	Px, plg, bio, qtz, mt, chl	Moderate
7647-C	Dacite	978A-47R-1, 0-6	—	—	—	10	1	1	—	—	<1	—	—	—	Plg, amph, bio, qtz, mt, chl, ep	Moderate
7647-E	Dacite	978A-47R-1, 0-6	—	<1	—	15	—	—	—	<1	1	—	—	—	Px, plg, qtz, mt, chl	Moderate
7647-M	Dacite	978A-47R-1, 0-6	—	—	—	10	—	3	—	10	—	—	—	—	Plg, qtz, mt, chl, ep	Moderate
7647-V	Dacite	978A-47R-1, 0-6	—	—	—	15	—	2	—	—	<1	—	—	—	Plg, mt, chl, ep	Moderate
7647-X	Dacite	978A-47R-1, 0-6	—	<1	<1	10	2	—	—	2	2	—	—	—	Opx, plg, qtz, mt, chl, ep	Moderate
7648	Dacite	977A-63X-1, 5-11	—	—	—	10	3	3	—	5	—	—	—	—	Plg, qtz, mt, chl	Moderate
7521	Rhyolite	977A-60X-1, 0-7	—	—	—	5	—	1	1	1	—	—	—	—	Plg, bio, qtz, mt, chl, ep	Slight
7522	Rhyolite	977A-61X-1, 0-7	—	—	—	10	—	3	1	1	—	—	—	—	Plg, bio, qtz, mt, ep	Slight
7646	Granite	977A-62X-1, 9-13	Alkali feldspar (55%), quartz (25%), plagioclase (10%), biotite (10%)													
7647-H	Metabasalt	978A-47R-1, 0-6	Actinolite (60%), quartz and feldspar (40%)													
7647-I	Metarhyolite	978A-47R-1, 0-6	Quartz (65%), muscovite (10%), feldspar (3%), Fe-ore (2%), vein calcite (20%)													
7647-U	Metadacite	978A-47R-1, 0-6	Quartz (70%), biotite (15%), Fe-ore (10%), feldspar (5%)													

Notes: Ol = olivine, px = pyroxene, cpx = clinopyroxene, opx = orthopyroxene, plg = plagioclase, amph = amphibole, bio = biotite, alk = alkali, fsp = feldspar, qtz = quartz, mt = magnetite, pyr = pyrite, cc = calcite, act = actinolite, chl = chlorite, ep = epidote. Actinolite, chlorite, and epidote are secondary phases. Both primary and secondary quartz occurs. — = no phenocrysts were present in thin section.

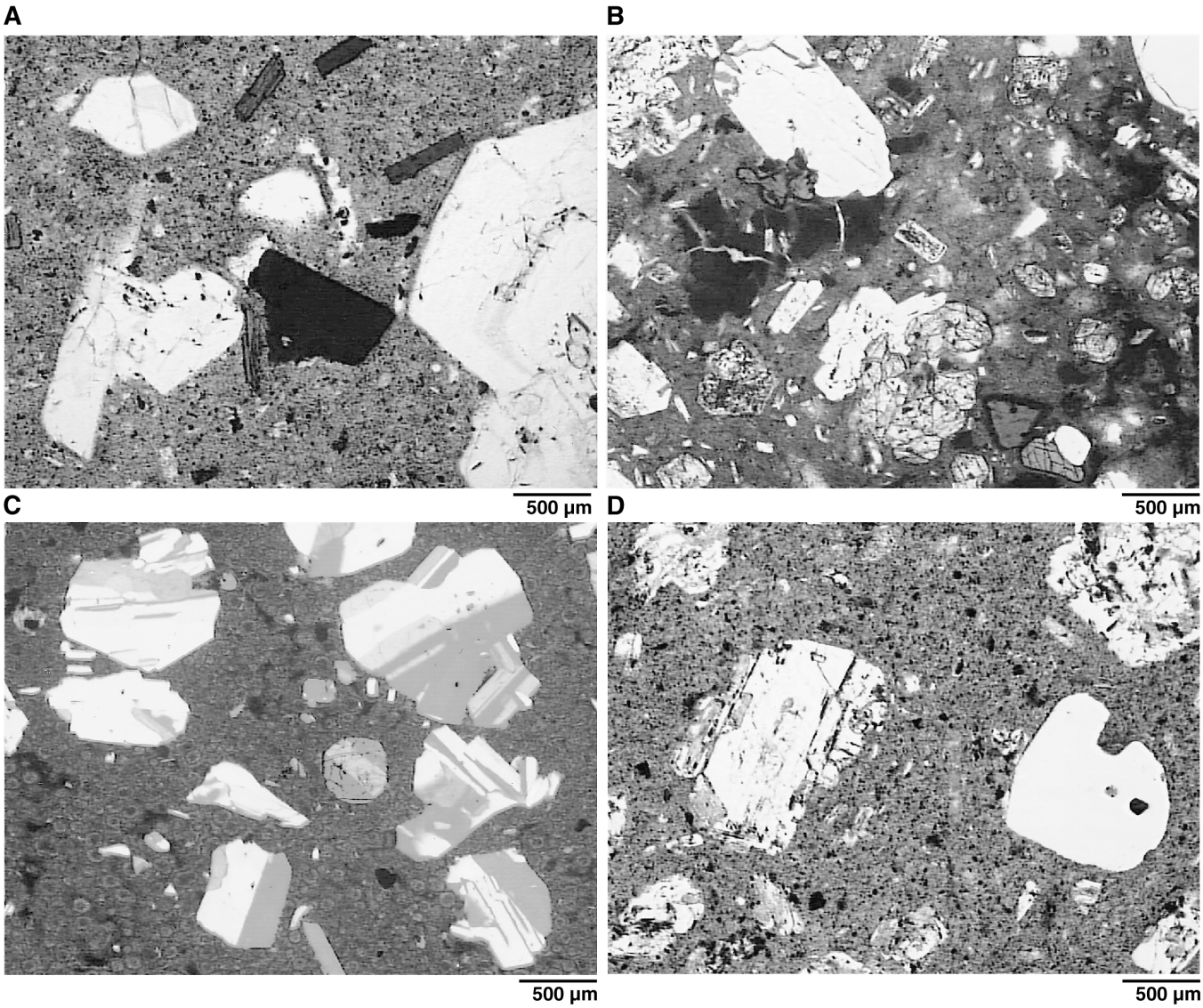

Figure 4. Photomicrograph of representative samples depicting the petrographic composition and degree of freshness/alteration of volcanic clastic fragments. **A.** Rhyolite 7522 (161-977A-61X-1, 0–7 cm) with phenocrysts of plagioclase, quartz and biotite in a microcrystalline matrix. **B.** Vitric groundmass with plagioclase, clinopyroxene, and titanomagnetite phenocrysts in basalt sample 7523 (161-977A-62X-1, 13–19 cm). **C.** Devitrified matrix with fresh phenocrysts of plagioclase and clinopyroxene in basaltic andesite 7519 (978A-46R-1, 4–9 cm). **D.** Dacite 7524 (977A-63X-1, 0–5 cm) with corroded quartz phenocrysts and partially altered plagioclase phenocrysts in microcrystalline matrix.

on plagioclase, sanidine, amphibole, and biotite phenocrysts from volcanic rocks covering the spectrum from basalt to rhyolite. Age determination results are presented in Table 4.

Dacite 7525 (161-978A-47R-1, 0–6 cm)

Eleven plagioclase phenocrysts (0.134–0.387 mg) from dacite 7525 were dated by single-crystal $^{40}Ar/^{39}Ar$ analysis. Apparent ages range from 5.5 ± 1.2 Ma to 8.5 ± 0.6 Ma. Isotope correlation returns a scatterchron with an age of 6.5 ± 0.4 Ma, and an initial $^{40}Ar/^{39}Ar$ ratio of 293 ± 4 (mean squared weighted deviate [MSWD] = 3.8; Fig. 5A). If the oldest crystal is excluded, the subpopulation yields an isochron age of 6.4 ± 0.3 Ma (MSWD = 1.63) and a mean apparent age of 6.1 ± 0.3 Ma (MSWD = 2.45), which is considered here the best estimate of the eruption age of dacite 7525.

Rhyolite 7521 (161-977A-60X-1, 0–7 cm)

Nine plagioclase phenocrysts, one sanidine phenocryst, and one biotite phenocryst (0.250–0.800 mg) from rhyolite 7521 were analyzed by single-crystal fusion. With apparent single-crystal ages ranging from 9.39 ± 0.18 Ma to 9.98 ± 0.30 Ma, the plagioclase analyses define an isochron with an age of 9.46 ± 0.11 Ma (MSWD = 1.32; Fig. 5A), and yield a mean apparent age of 9.55 ± 0.49 Ma. Their initial $^{40}Ar/^{39}Ar$ ratio is determined as 307 ± 12, identical to the atmospheric ratio of 295.5 within 1-σ error limits. A step-heating analysis of a single biotite phenocryst from the same sample gave an errorchron of 9.41 ± 0.10 Ma (MSWD = 6.88) and an integrated age for individual heating steps of 9.49 ± 0.05 Ma (Fig. 5B), which is identical to the plagioclase ages within error limits. A single sanidine phenocryst yields the most precise age estimate for the eruption of

rhyolite 7521. Its apparent age of 9.25 ± 0.02 Ma overlaps within error limits with the results obtained from plagioclase phenocrysts, but not with the poorly defined biotite errorchron.

Rhyolite 7522 (161-977A-61X-1, 0–7 cm)

Plagioclase phenocrysts from rhyolite 7522 (10 single-crystal analyses; 0.190–0.611 mg) give apparent ages ranging from 9.37 ± 0.07 Ma to 9.99 ± 0.12 Ma. The data are isochronous at 9.51 ± 0.14 Ma (MSWD = 2.71) and have a slightly elevated initial $^{40}Ar/^{39}Ar$ ratio of 341 ± 31 (Fig. 5A). The step-heating analysis of a biotite phenocryst gives an isochron age of 9.29 ± 0.10 Ma, a near-atmospheric initial $^{40}Ar/^{39}Ar$ ratio of 296 ± 12, and an MSWD of 1.64. The age spectrum is flat but does not represent a plateau region (sensu stricto) within 1-σ error limits (Fig. 5B). The integrated age is 9.25 ± 0.05 Ma. The best estimate of the eruption age of rhyolite 7522 is again derived from a single sanidine crystal analysis. Its apparent age of 9.29 ± 0.02 Ma agrees with the biotite step-heating results, but is significantly younger than the poorly defined plagioclase data.

Table 2. Standard data for XRF-measurement.

Sample	RGM-1	BM (*N* = 7)	SY-2 (*N* = 10)	SDC-1 (*N* = 11)
Major elements (wt%)				
SiO_2	73.51	49.76	60.3	66.08
TiO_2	0.27	1.14	0.14	1
Al_2O_3	13.8	16.35	12.19	15.98
Fe_2O_3	1.67	9.67	6.08	6.9
MnO	0.64	0.15	0.32	0.12
MgO	0.27	7.66	2.75	1.75
CaO	1.18	6.35	7.89	1.41
Na_2O	4.09	5.12	4.5	2.08
K_2	4.31	0.17	4.48	3.27
P_2O_5	0.66	0.12	0.43	0.15
Trace elements (ppm)				
Ba	822	265	444	636
Rb	153	8	206	127
Sr	105	226	272	181
Zr	222	1000	299	328
V	16	202	49	97
Cr	<18	130	<18	53
Co	<4	42	10	18
Ni	5	60	10	28
Cu	35	46	6	29
Zn	33	120	243	100
Ga	15	20	29	23

Table 3. Standard and blank data for ICP-MS.

Sample	Blank I (ppb)	Blank II (ppb)	BHVO (ppm)	RGM-1 (ppm)	STM-1 (ppm)
Pb	0.038	0.135	2.1	23.5	17.2
Th	0.004	0.003	1.25	1.5	32
U	0.001	0.001	0.446	5.95	9.28
Hf	0.001	0.001	4.86	6.31	30.3
Nb	0.003	0.004	17.1	8.2	254
Ta	0.001	0.002	1.1	0.84	16.5
Y	0.003	0.000	24.3	20.9	42.3
La	0.000	0.004	16.1	23.7	158
Ce	0.002	0.009	39	46.9	276
Pr	0.000	0.001	5.64	5.41	27.1
Nd	0.001	0.004	25.3	19.3	83.2
Sm	0.001	0.000	6.49	4.07	13.1
Eu	0.000	0.000	2.16	0.609	3.58
Gd	0.002	0.002	6.4	3.8	10.2
Tb	0.000	0.000	1	0.621	1.56
Dy	0.000	0.000	5.63	3.79	8.46
Ho	0.000	0.000	1.04	0.774	1.59
Er	0.000	0.000	2.58	2.3	4.4
Tm	0.000	0.000	0.349	0.377	0.675
Yb	0.000	0.001	2.1	2.56	4.51
Lu	0.000	0.000	0.296	0.395	0.665

Basalt 7523 (161-977A-62X-1, 13–19 cm)

Seven amphibole phenocrysts (0.060–0.261 mg) were dated from basalt 7523 (Fig. 5A). With single-crystal apparent ages ranging from 8.8 ± 2.9 Ma to 11.8 ± 1.6 Ma, the analyses yield an isochron age of 9.95 ± 0.64 Ma and an initial $^{40}Ar/^{39}Ar$ ratio of 294 ± 10 (MSWD = 0.94). Isochron and mean apparent ages (9.90 ± 0.40 Ma) are identical within error limits, but analytical precision is low because of small sample masses, low potassium content (i.e., insufficient neutron dose), and high nonradiogenic argon contents.

Dacite 7524 (161-977A-63X-1, 0–5 cm)

Plagioclase phenocrysts from dacite 7524 (six single-crystal analyses; 0.162–0.563 mg) give apparent ages ranging from 11.1 ± 1.3 Ma to 13.8 ± 0.3 Ma (Fig. 5A). This population yields a scatterchron age of 12.5 ± 0.9 Ma with an initial $^{40}Ar/^{39}Ar$ ratio of 303 ± 13 (MSWD = 7.1). The mean apparent age (13.0 ± 0.3 Ma) is poorly constrained as well; its high MSWD (6.1) indicates the presence of different age populations in the crystal assemblage analyzed. Excluding two crystals with apparent ages of 13.5 ± 0.2 Ma and 13.8 ± 0.3 Ma drastically decreases the MSWD (0.36) and yields a mean apparent age of 12.1 ± 0.2 Ma. It is not clear whether the observed scatter in the plagioclase population of 7524 and 7525 reflects loss of radiogenic ^{40}Ar from some of the apparently younger crystals because of alteration or thermal overprinting, or whether it indicates the presence of older xenocrysts in these magmas.

In summary, the single-crystal and step-heating laser $^{40}Ar/^{39}Ar$ analyses of plagioclase, sanidine, biotite, and amphibole phenocrysts from lava clasts in Cores 161-977A-60X–63X and 978A-47R indicate that the eruptions of these basaltic to rhyolitic magmas occurred between 6.1 (dacite 7525) and 12.1 Ma (dacite 7524). At Hole 977A, the eruption ages of the volcanic rocks studied, systematically increase with depth and thus conform to the stratigraphy (i.e., from Core 60X [9.25 Ma], to Core 61X [9.29 Ma], to Core 62X [9.9 Ma] and Core 63X [12.1 Ma]). A clast from Core 60X was assigned to Zone NN7 (~10.6–12.2 Ma) within the Serravallian, based on the mi-

Table 4. Results of $^{40}Ar/^{39}Ar$ laser dating.

Core, section, interval (cm)	Sample	Mineral	*N*	Type	Age (Ma)	Error (1σ)	MSWD	Isochron age (Ma)	Error (1σ)	Initial $^{40}Ar/^{36}Ar$	Error (1σ)	MSWD
161-977A-60X-1, 0-7	7521	Plagioclase	9	SX-MAA	9.55	0.49	1.64	9.46	0.11	307	12	1.32
977A-60X-1, 0-7	7521	Sanidine	1	SX-A	9.25	0.02						
977A-60X-1, 0-7	7521	Biotite	14	SH-IA	9.49	0.05		9.41	0.10	298	5	6.88
977A-61X-1, 0-7	7522	Plagioclase	10	SX-MAA	9.70	0.07	3.98	9.51	0.14	341	31	2.71
977A-61X-1, 0-7	7522	Sanidine	1	SX-A	9.29	0.02						
977A-61X-1, 0-7	7522	Biotite	7	SH-IA	9.25	0.05		9.29	0.10	296	12	1.64
977A-62X-1, 13-19	7523	Amphibole	7	SX-MAA	9.90	0.40	0.80	9.95	0.64	294	10	0.94
977A-63X-1, 0-5	7524	Plagioclase	6	SX-MAA	13.00	0.30	6.10	12.47	0.92	303	13	7.06
			4	SX-MAA	12.10	0.20	0.36					
978A-47R-1, 0-20	7525	Plagioclase	11	SX-MAA	6.20	0.30	3.60	6.50	0.40	293	4	3.80
			10	SX-MAA	6.10	0.30	2.45	6.40	0.30	290	3	1.63

Note: SX-MAA = single crystal mean apparent age, SX-A = single crystal apparent age, SH-IA = step-heating integral age, N = number of single crystal analyses for SX, number of heating steps for SH, MSWD = mean square weighted deviates.

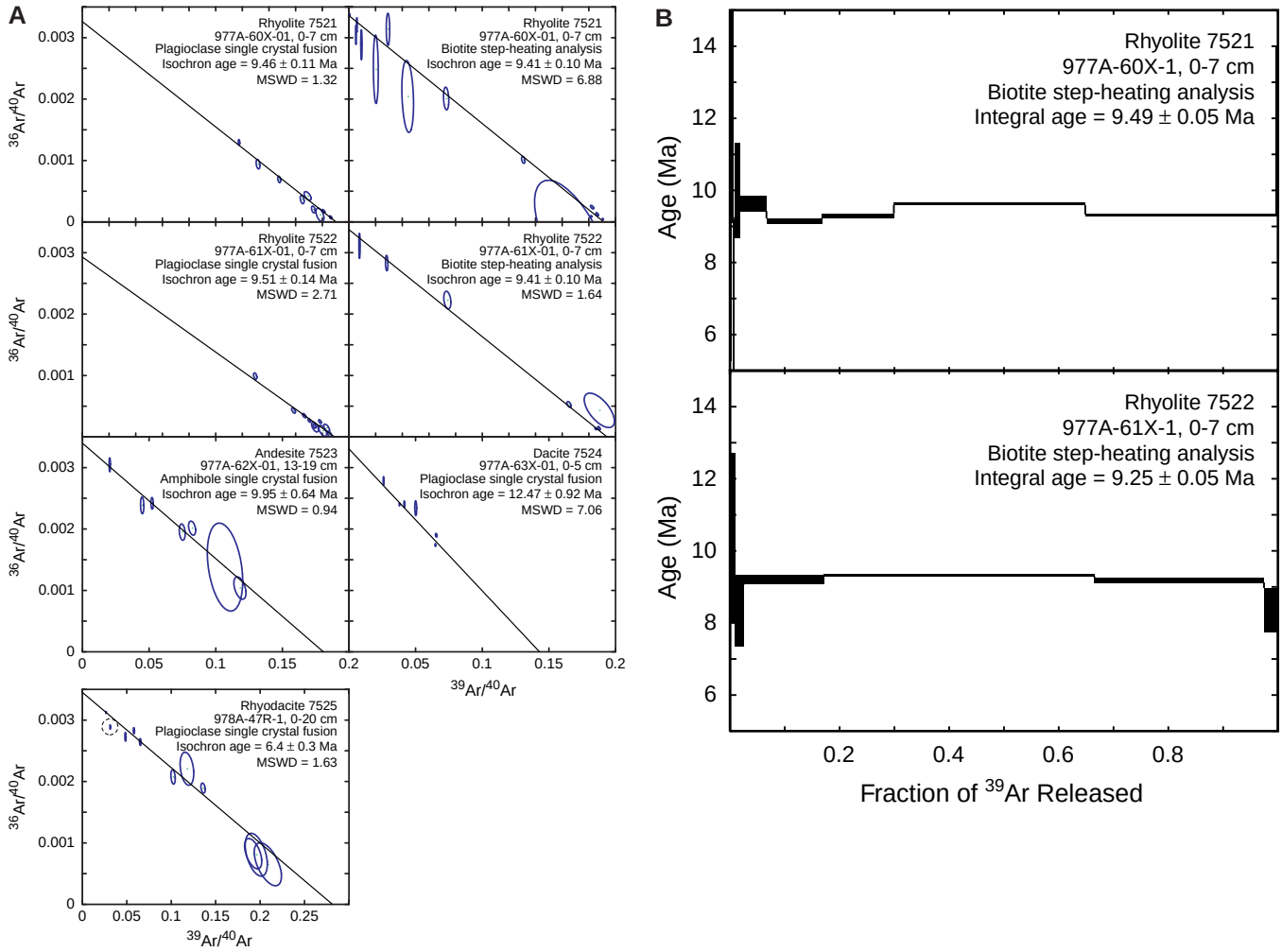

Figure 5. **A.** Inverse isochron diagrams show the best-fit regression lines. Argon isotope ratios of single plagioclase and amphibole phenocrysts, and biotite step-heating are shown with 1-σ error ellipses. Analyses are normalized to a common J-value of 1×10^{-4}. Dashed encircled points are excluded from regressions. **B.** Age spectrum diagrams showing the results of laser step-heating analyses of biotite crystals from rhyolites 7521 and 7522. Mean apparent ages of heating steps are shown with 1-σ error bars.

crofossil assemblage scraped from this sample (Comas, Zahn, Klaus, et al., 1996). This provides further support for a mid-Miocene age for the base of Hole 977A. Sample 161-978A-47R–1, 0–6 cm (7525), also has an age similar to that of microfossils from the same unit (6.52 Ma; Comas, Zahn, Klaus, et al., 1996). These observations are consistent with deposition of the volcanic clasts shortly after their eruption and suggests that at least some of the pebbles were derived from local volcanic structures, such as Al-Mansour Seamount, Yusuf Ridge, and Maimonides Ridge (?).

MAJOR- AND TRACE-ELEMENT GEOCHEMISTRY

Major- and trace-element compositions for 24 whole-rock samples (eight samples from Site 977 and 16 from Site 978) are reported in Table 5. The samples from both sites range in composition from basalt to rhyolite (Fig. 6A) and belong to the tholeiitic, calc-alkaline, high-K calc-alkaline, and shoshonite series (Fig. 6B). The samples show a greater range in chemical composition than those from Cabo de Gata and extend to more mafic compositions (Fig. 6A).

As is illustrated in Figure 7, the major elements and compatible trace elements show systematic variations of SiO_2 content. Relatively immobile elements, such as Al_2O3, FeO* (total iron as FeO), TiO_2, V, Co, and Cr, decrease with increasing SiO_2. Dacite sample 7647-U (161-978A-47R-1, 0–6 cm) has elevated TiO_2 and FeO*, which probably reflect the large amount of titanomagnetite in this sample (~10%). If the four samples with $H_2O > 4$ are excluded, then CaO, CaO/Al_2O_3, MgO, P_2O_5, and Sr show inverse correlations with SiO_2. In the four samples with $H_2O > 4$, the higher MgO, but lower CaO, CaO/Al_2O_3, P_2O_5, and Sr than in the other samples at similar SiO_2, most likely reflect the effects of seawater alteration, consistent with the greater degree of alteration observed in the thin sections of these samples. Sample 7647-H (161-978A-47R-1, 0–6 cm) has anomalously low Al_2O_3, TiO_2, and Sr and anomalously high CaO/Al_2O_3 and MgO (Table 5). Most incompatible elements show crude positive correlations with SiO_2, but correlate much better with each other (Fig. 8).

Compared to both mid-ocean ridge basalt (MORB) and ocean-island basalt (OIB), basaltic samples from the Alboran have high ratios of "fluid-mobile" (also often referred to as the large-ion-lithophile elements [LILE]) to "fluid-immobile" (Th, high-field-strength elements [HFSE], and REE) elements (e.g., Ba/Nb [21–65], Ba/Ta [248–870], Ba/La [7–34], K/Nb [617–10,917], K/Ta [7308–127,077]), and of light (L)REE to HFSE (e.g., La/Nb [1.0–6.2] and

Table 5. Major- and trace-element analyses.

Sample:	161-978A-46R-1	978A-46R-1	978A-46R-1	978A-47R-1	978A-47R-1	978A-47R-1	978A-47R-1	978A-47R-1	978A-47R-1	978A-47R-1	978A-47R-1	978A-47R-1	978A-47R-1	978A-47R-1	978A-47R-1	978A-47R-1	977A-60X-1	977A-60X-1	977A-61X-1	977A-62X-1	977A-62X-1	977A-62X-1	977A-63X-1	977A-63X-1
Interval (cm):	4-9	4-9	4-9	0-6	0-6	0-6	0-6	0-6	0-6	0-6	0-6	0-6	0-6	0-6	0-6	0-6	0-7	27-31	0-7	4-9	9-13	13-19	0-5	5-11
Internal sample no.:	7519	7519-II	7525	7647-B	7647-C	7647-E	7647-H	7647-I	7647-K	7647-M	7647-O	7647-Q	7647-U	7647-V	7647-X	7518	7521	7520	7522	7649	7646	7523	7524	7648
Major elements (wt%)																								
SiO_2	52.51	59.46	67.52	53.68	66.15	63.50	52.56	68.13	56.85	64.78	53.80	41.37	66.25	66.61	64.63	47.74	72.93	52.68	72.11	53.29	70.46	49.41	67.83	68.80
TiO_2	0.76	0.53	0.40	0.88	0.50	0.49	0.23	0.37	0.52	0.47	0.61	0.59	0.75	0.35	0.46	0.73	0.23	0.57	0.22	0.64	0.24	0.77	0.40	0.30
Al_2O_3	21.9	17.06	14.94	16.49	15.78	15.64	7.76	4.52	17.28	16.51	14.93	17.01	13.90	15.39	15.57	18.37	14.17	16.17	14.40	16.65	15.13	18.29	14.37	15.17
FeO^t	6.23	6.35	3.89	8.11	3.80	5.14	9.99	1.19	5.27	3.16	7.88	7.86	5.11	4.70	4.72	8.22	1.76	8.13	1.94	7.14	2.25	7.85	4.11	2.81
MnO	0.04	0.04	0.05	0.16	0.06	0.11	0.21	0.14	0.10	0.05	0.11	0.05	0.08	0.05	0.04	0.13	0.01	0.12	0.02	0.05	0.04	0.07	0.07	0.05
MgO	2.00	1.72	1.38	5.46	2.68	3.43	13.04	1.86	6.48	1.32	4.52	3.49	2.01	1.22	2.33	8.29	0.48	10.93	0.48	8.99	1.44	6.48	2.63	1.68
CaO	9.43	6.72	3.64	9.51	4.13	4.47	11.42	11.73	3.35	4.48	5.01	7.43	5.39	4.24	5.01	4.61	1.70	0.98	1.72	0.74	2.77	10.56	2.92	2.82
Na_2O	3.43	2.84	3.33	2.65	2.58	2.32	1.20	2.26	3.14	2.79	2.90	2.73	0.86	3.84	2.90	2.07	3.57	3.58	3.61	0.83	2.48	2.70	2.76	2.59
K_2O	0.41	2.57	3.15	0.34	2.76	1.68	0.37	0.22	1.80	3.88	3.58	0.55	2.26	1.22	1.99	1.97	4.62	0.07	4.60	4.39	3.86	0.28	1.65	3.89
P_2O_5	0.156	0.264	0.174	0.086	0.087	0.072	0.023	0.079	0.065	0.103	0.097	0.329	0.138	0.096	0.077	0.076	0.067	0.055	0.066	0.049	0.081	0.147	0.051	0.089
H_2O	2.02	1.25	0.94	1.84	2.14	2.59	2.13	0.43	4.50	1.10	—	3.21	1.53	—	1.75	6.21	0.53	6.06	0.32	6.22	0.95	2.06	2.48	1.19
CO_2	0.09	0.11	0.18	0.13	0.14	0.74	0.12	9.88	1.20	0.75	—	0.40	1.15	—	0.26	1.46	0.03	0.13	0.02	0.23	0.06	0.18	0.08	0.13
Total	98.98	98.91	99.59	99.34	100.81	100.18	99.05	100.81	100.56	99.39	93.44	85.02	93.43	97.72	99.74	99.88	100.10	99.48	99.51	99.22	99.76	98.80	99.35	99.52
Trace elements (ppm)																								
Ba	93	717	912	108	369	268	12	45	133	345	748	336	312	105	198	92	880	<8	897	36	168	82	65	208
Rb	9	90	117	15	106	36	8	9	25	140	48	9	108	69	86	19	167	<4	171	20	245	<4	11	225
Sr	298	326	268	163	124	95	28	515	88	145	139	436	201	126	99	104	187	61	194	55	82	385	66	91
Pb*	3.45	4.38	4.82	4.87	6.95	3.34	0.415	3.92	4.79	15.5	4.49	4.89	27.9	3.55	9.26	9.00	12.68	2.01	13.2	2.30	65.9	2.60	1.53	57.1
Th*	4.27	14.1	24.3	0.925	10.7	3.61	0.096	8.54	2.24	8.92	6.46	12.7	11.9	2.95	2.66	1.37	18.6	0.233	19.2	0.365	8.48	6.58	0.757	9.84
U*	1.22	4.72	7.21	0.463	1.99	0.822	0.087	1.64	1.48	2.33	0.332	3.16	2.85	1.14	0.737	1.09	6.59	0.376	6.95	2.07	2.48	3.18	0.619	3.06
Zr	73	100	157	70	131	87	16	325	62	121	127	64	216	93	100	53	178	30	177	32	74	83	81	88
Hf*	2.29	3.02	4.39	1.47	1.05	2.53	0.374	1.78	1.54	0.616	2.18	2.22	5.40	2.77	1.04	1.78	3.21	0.683	3.06	0.993	0.826	2.56	2.10	0.680
Nb*	3.37	6.92	8.78	2.60	8.08	2.63	0.291	6.32	1.78	7.51	6.07	5.19	11.2	2.07	2.87	2.45	10.5	0.449	11.1	0.556	10.4	3.91	0.819	9.97
Ta*	0.272	0.510	0.621	0.194	0.680	0.210	0.025	0.439	0.175	0.650	0.508	0.386	0.920	0.149	0.235	0.159	0.968	0.039	0.981	0.043	1.70	0.330	0.068	1.50
Y*	16.1	13.8	18.7	18.2	19.3	17.1	8.03	16.4	17.0	16.0	17.4	23.9	30.0	23.4	14.5	17.8	17.4	7.34	22.3	17.8	10.7	20.9	18.0	13.8
La*	12.2	23.6	25.4	3.27	29.3	8.75	0.355	24.2	6.24	25.6	12.2	32.1	36.6	8.84	11.4	5.83	44.3	0.464	48.1	2.44	13.3	12.6	3.00	17.6
Ce*	27.2	46.9	53.4	9.31	58.1	18.3	1.00	54.4	12.6	52.0	22.2	67.8	75.6	19.7	22.5	13.3	88.6	1.39	96.0	6.70	28.2	39.7	8.16	36.7
Pr*	3.71	5.62	6.64	1.49	6.59	2.26	0.177	6.79	1.62	6.11	3.21	8.56	8.44	2.72	2.65	1.85	10.0	0.245	11.0	1.11	3.26	4.06	1.31	4.28
Nd*	15.2	21.7	26.1	7.28	24.0	8.95	1.00	26.1	6.87	22.4	13.3	33.2	33.1	12.0	10.1	8.11	35.4	1.41	39.0	5.85	11.8	17.3	6.50	15.7
Sm*	3.80	4.36	5.33	2.36	4.82	2.33	0.515	5.05	2.04	4.78	3.11	7.28	6.19	3.23	2.39	2.39	6.58	0.571	7.19	2.12	2.95	4.60	2.19	3.67
Eu*	1.10	1.05	1.14	0.830	1.05	0.604	0.159	0.863	0.642	0.967	0.870	1.55	1.20	0.961	0.675	0.676	1.16	0.227	1.28	0.689	0.628	1.20	0.573	0.660
Gd*	3.66	3.45	4.18	2.92	4.31	2.63	0.827	3.90	2.54	4.08	3.11	6.12	6.66	3.57	2.53	2.85	5.01	0.838	5.69	2.65	2.66	4.60	2.52	3.30
Tb*	0.598	0.501	0.617	0.541	0.668	0.480	0.186	0.595	0.475	0.619	0.520	0.917	0.905	0.637	0.450	0.534	0.714	0.177	0.832	0.497	0.419	0.755	0.472	0.521
Dy*	3.47	2.80	3.54	3.56	3.84	3.17	1.35	3.26	3.17	3.38	3.32	5.10	4.97	4.09	2.80	3.49	3.76	1.32	4.50	3.39	2.23	4.46	3.13	2.89
Ho*	0.666	0.550	0.718	0.753	0.748	0.677	0.312	0.624	0.681	0.624	0.707	0.963	1.04	0.886	0.578	0.742	0.708	0.312	0.868	0.748	0.402	0.846	0.687	0.529
Er*	1.72	1.52	2.09	2.11	2.03	1.97	0.924	1.68	1.92	1.61	2.13	2.44	2.62	2.57	1.60	2.08	1.90	0.955	2.39	2.20	1.09	2.16	2.03	1.45
Tm*	0.234	0.228	0.332	0.315	0.297	0.312	0.151	0.248	0.301	0.222	0.371	0.320	0.387	0.404	0.240	0.321	0.271	0.156	0.355	0.338	0.163	0.286	0.327	0.218
Yb*	1.41	1.55	2.31	2.04	1.86	2.15	1.03	1.61	1.98	1.39	2.99	1.89	2.61	2.70	1.59	2.10	1.76	1.06	2.34	2.26	1.08	1.68	2.26	1.36
Lu*	0.188	0.234	0.361	0.297	0.269	0.332	0.165	0.238	0.304	0.191	0.514	0.258	0.368	0.424	0.240	0.309	0.250	0.157	0.343	0.346	0.152	0.228	0.354	0.196
V	229	163	61	230	100	124	208	19	165	104	157	224	107	39	115	232	18	233	17	272	44	262	112	57
Cr	<18	<18	<18	<18	40	19	207	<18	117	<18	54	33	75	<18	<18	47	<18	130	<18	124	<18	176	<18	<18
Co	10	13	6	32	12	14	47	<4	13	7	15	14	19	6	14	64	<4	35	<4	25	7	20	13	8
Ni	<2	3	11	15	4	<2	139	<2	28	3	11	18	29	<2	<2	51	<2	44	<2	60	3	26	<2	<2
Cu	50	26	11	13	17	15	37	<4	22	11	22	120	22	10	47	76	<4	28	<4	116	16	48	39	8
Zn	69	57	37	63	33	98	41	18	94	41	64	115	86	146	53	87	21	93	16	44	42	63	55	41
Ga	20	16	16	13	19	16	11	<8	17	21	16	12	21	18	17	17	20	11	23	21	13	22	16	18

Notes: Data from ICP-MS is denoted with *, all other data from XRF. ICP-MS data reflect averages of duplicate analyses. — = no data available.

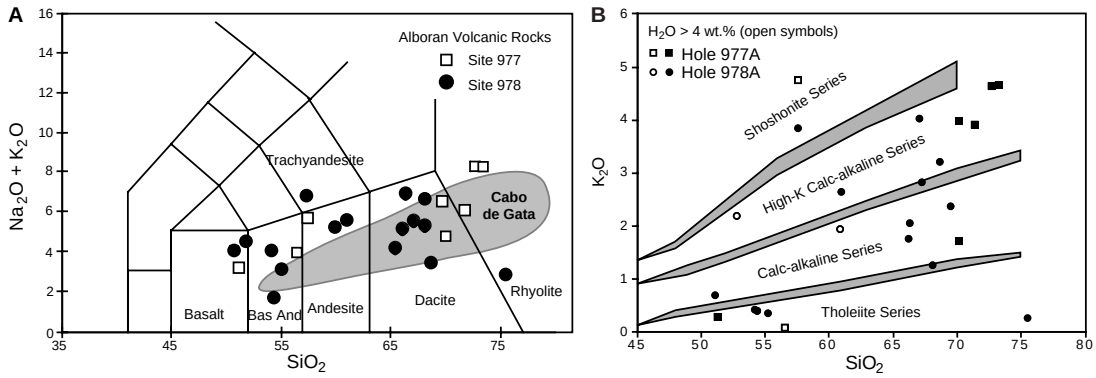

Figure 6. Volcanic rocks from Sites 977 (squares) and 978 (circles). **A.** SiO_2 vs. total alkalis ($Na_2O + K_2O$) after Le Maitre et al. (1989). Also shown are data for Cabo de Gata (shaded field) from Fernandez Soler (1992). Data were normalized to 100% on a volatile-free basis. **B.** SiO_2 vs. total K_2O after Rickwood (1989). The shaded regions denote the divisions between the tholeiite, calc-alkaline, high-K calc-alkaline, and shoshonite fields.

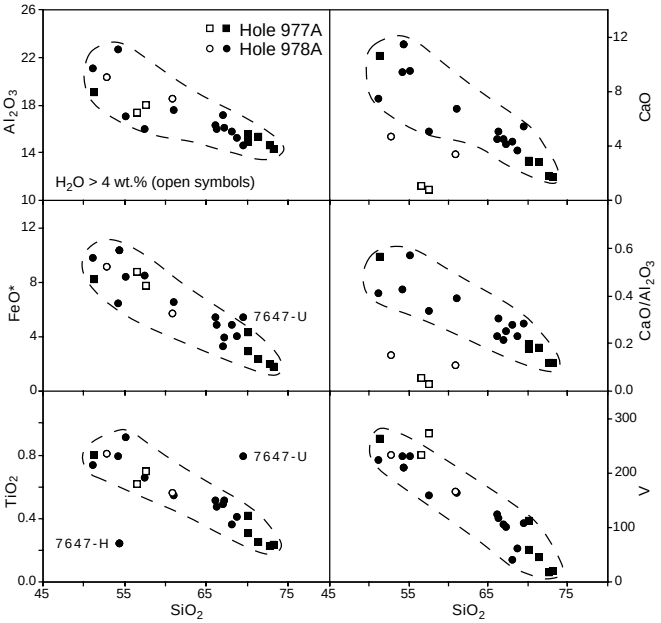

Figure 7. SiO_2 vs. Al_2O_3, CaO, FeO*, CaO/Al_2O_3, TiO_2, and V. Major-element data were normalized to 100% on a volatile-free basis, assuming that CO_2 comes from $CaCO_3$. Rhyolite sample 7647-I (161-978A-47R-1, 0–6 cm) was omitted from the diagram, because of its high CO_2 (9.9 wt%) content and thus causing a problem with the CaO correction. Dashed fields enclose data with $H_2O < 4$ wt%, except when sample name is noted.

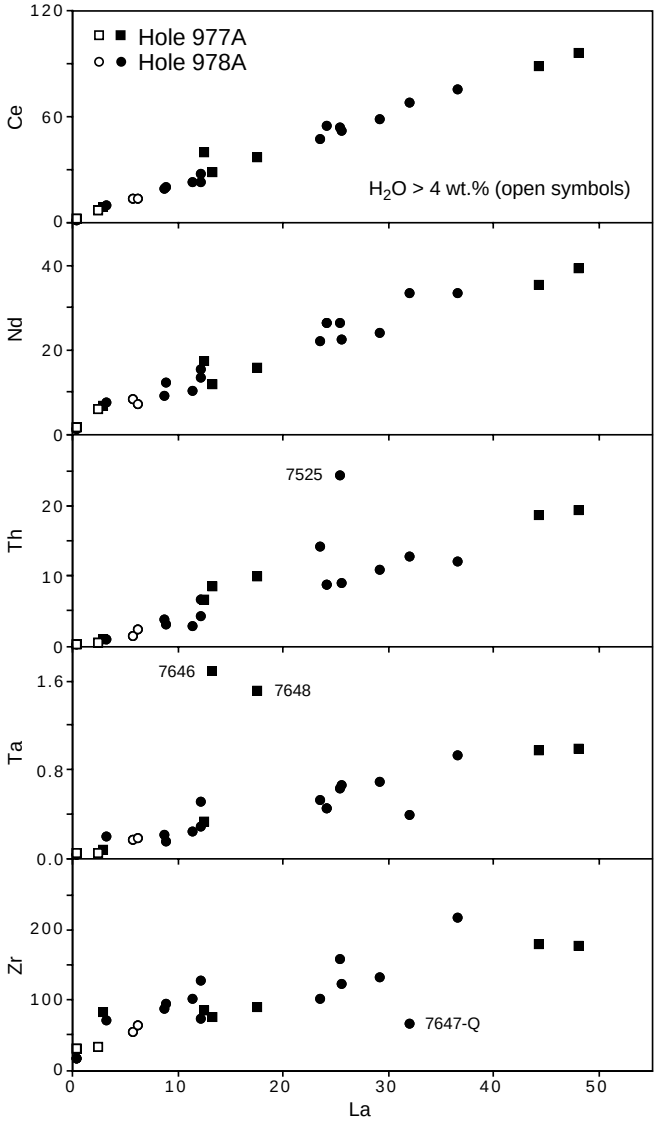

Figure 8. La vs. Ce, Nd, Th, Ta, and Zr. Immobile incompatible elements show good correlations with each other. Because the altered samples (open and solid symbols) fall on the trends defined by the fresher samples, alteration does not appear to have significantly affected the immobile incompatible-element abundances. Rhyolite sample 7647-I (161-978A-47R-1, 0–6 cm) with 9.9 wt% CO_2 has 325 ppm Zr and thus plots off the graph.

La/Ta [12–83]), but low ratios of immobile to mobile elements (e.g., Nb/U [1.2–5.6] and Ce/Pb [0.7–15]). The ratios in the Alboran samples, however, are characteristic of subduction-related volcanic rocks.

The REE patterns, normalized to chondrite using the values of Boynton (1984), are shown in Figure 9. The basalts and basaltic andesites can be divided into two groups based on their REE abundances: (1) the LREE-depleted group has patterns similar to those observed in normal (N) and enriched (E) MORB, and (2) the LREE-enriched group has patterns characteristic of OIB (e.g., basalts from Saint Helena and Gomera (Canary Islands; Fig. 9A). The LREE-depleted group contains Samples 7520 (161-977A-60X-1, 27–31 cm), 7647-H (978A-47R-1, 0–6 cm), 7647-B (978A-47R-1, 0–6 cm), and 7518 (978A-47R-1, 0–6 cm), and the LREE-enriched group contains samples 7647-Q (978A-47R-1, 0–6 cm), 7523 (977A-62X-1, 13–19 cm), and 7519 (978A-46R-1, 4–9 cm). The andesites, dacites, and rhyolites generally show LREE enrichment with $(La/Yb)_N \geq 1$.

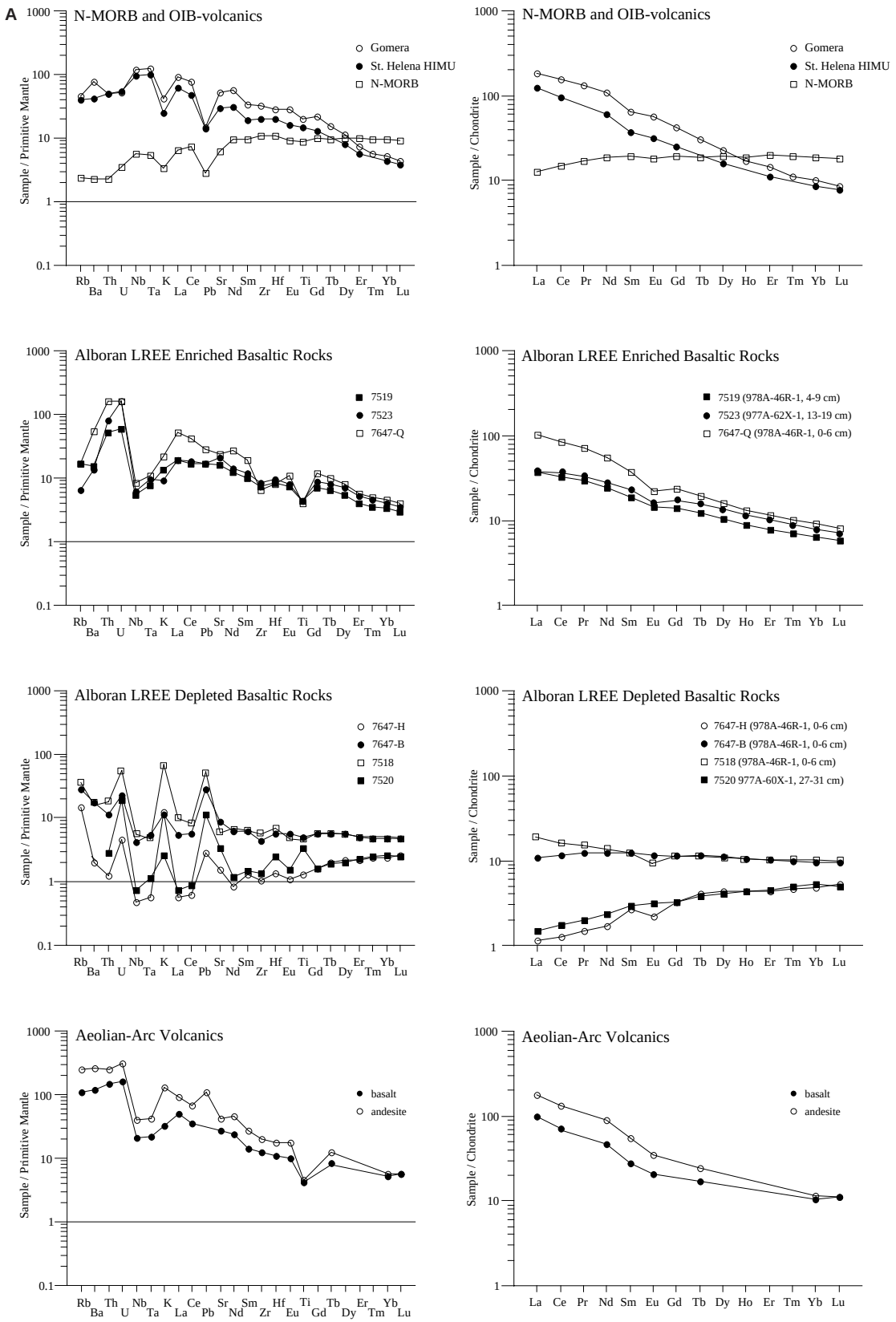

Figure 9. Multi-element diagrams for chondrite-normalized REEs (Boynton, 1984) and for incompatible elements normalized to primitive mantle (Hofmann, 1988). **A.** Data for Alboran basalts and basaltic andesites. (Continued next page.)

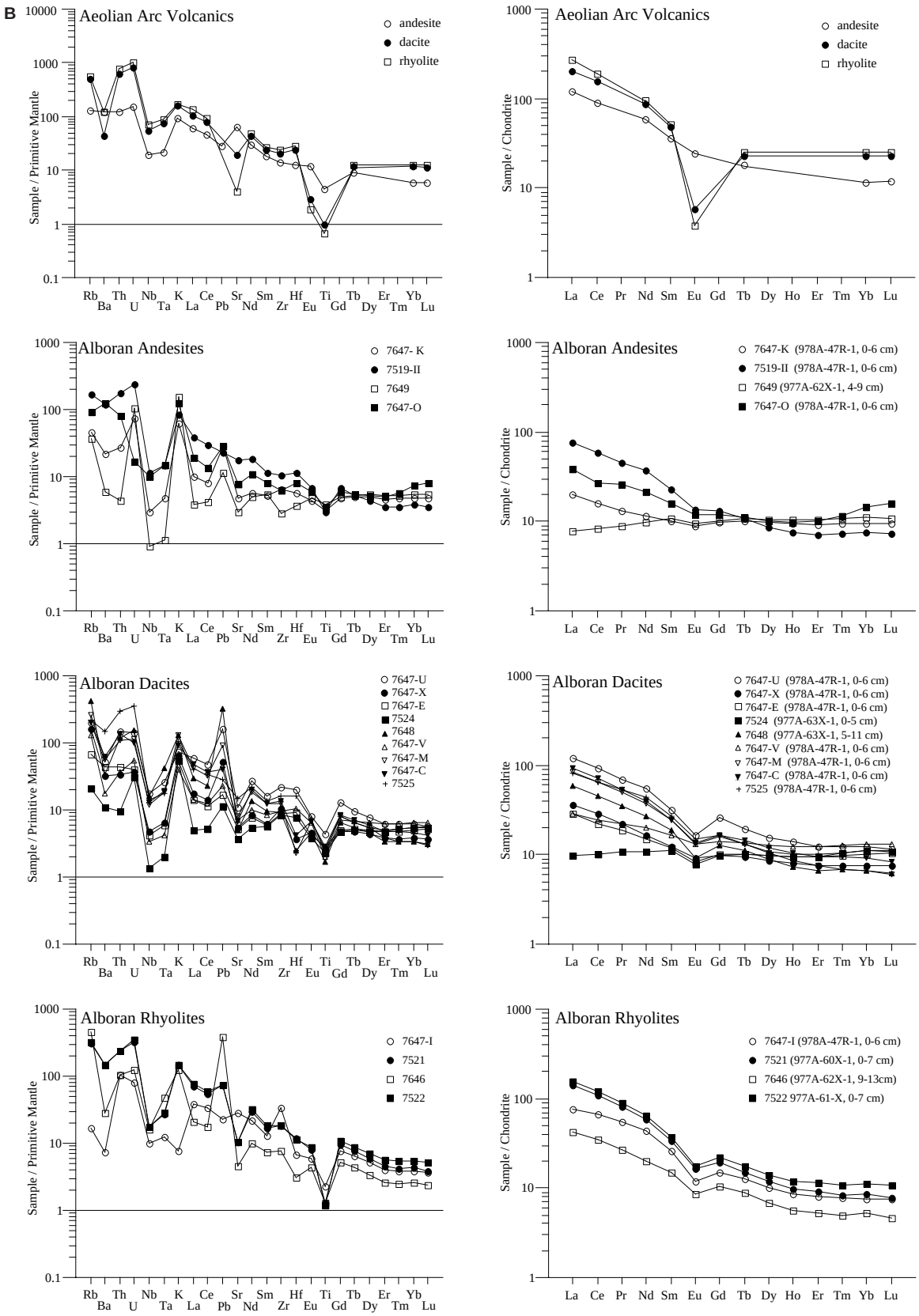

Figure 9 (continued). **B.** Data for Alboran andesites, dacites, and rhyolites. Average normal MORB (N-MORB; Hofmann, 1988), ocean island basalts from Saint Helena (Chaffey et al., 1989) and Gomera (S. Dorn and K. Hoernle, unpubl. data), and Aeolian Arc (Salina) basalts, andesite, dacite, and rhyolite (Ellam et al., 1989) are shown for comparison.

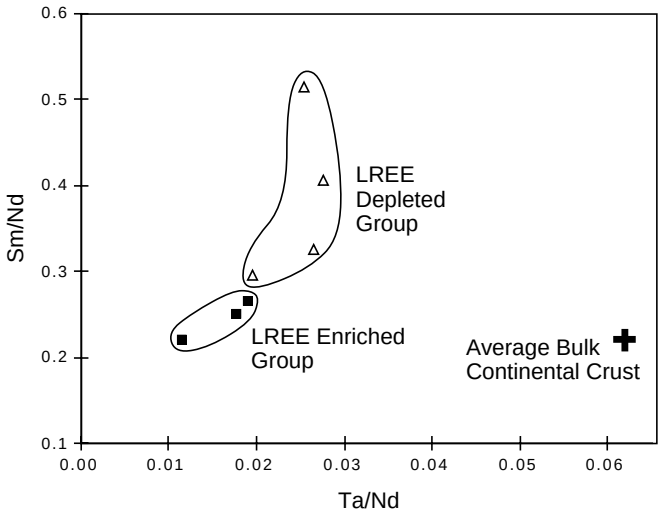

Figure 10. Variations in Ta/Nd and Sm/Nd between the LREE-enriched and LREE-depleted basaltic rocks from Sites 977 and 978 are not consistent with assimilation of continental crust (average bulk continental crust values from Taylor and McLennan, 1985).

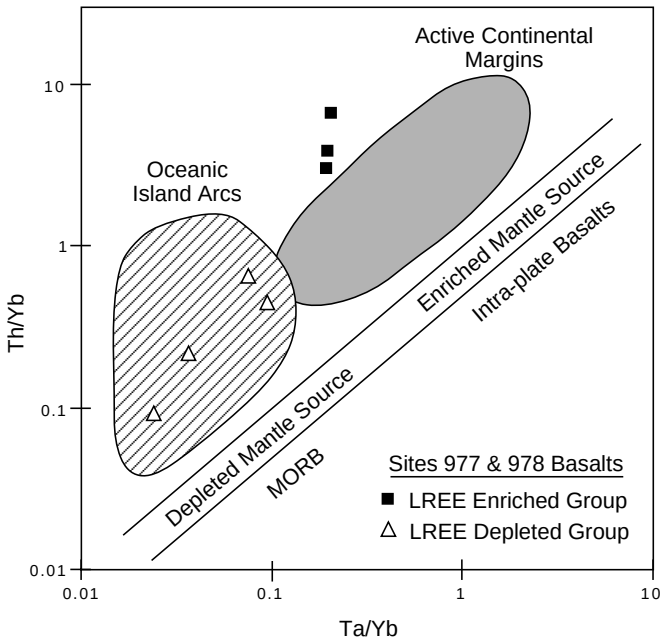

Figure 11. Ta/Yb vs. Th/Yb (after Pearce, 1983) for Alboran basaltic rocks from Sites 977 and 978, which illustrates the difference between the LREE-enriched and LREE-depleted groups. All basalts have clear subduction zone affinities.

Most samples, especially in the more evolved rock types, have negative Eu anomalies. The more evolved samples (andesites through rhyolites) typically have concave patterns, reflecting depletion of the middle (M)REEs.

The incompatible-element diagrams (Fig. 9), normalized to primitive mantle after Hofmann (1988), are strongly spiked. Pronounced troughs occur at Nb and Ta in all samples. Peaks occur in most, but not all samples, at U and Pb. In general, mobile elements, such as Rb, Ba, U, K, and Sr, are enriched relative to less mobile elements such as high field strength elements (HFSE, for example Nb, Ta, Zr, Hf)

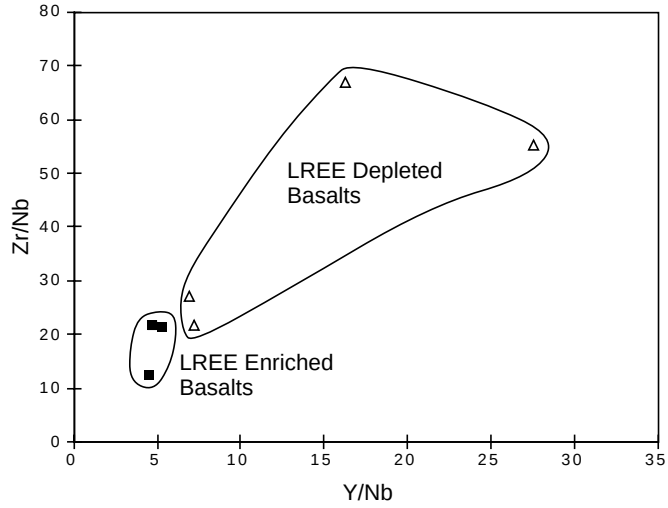

Figure 12. Y/Nb vs. Zr/Nb diagrams illustrate the difference between the LREE-enriched and LREE-depleted basalt groups from Sites 977 and 978.

and the REE. Th generally behaves similar to the LREEs (e.g., samples with high La have high Th and vice versa). The basalt groups also display distinct characteristics on multi-element diagrams (Fig. 9A). The LREE-enriched basalts are also characterized by relative enrichments in Th and U but depletions in Rb, Ba, K, Zr and Ti, as well as Nb and Ta. The LREE-depleted basalts show relative enrichments in Rb, U, K, Pb and Sr but relative depletion in Th, as well as in Nb and Ta.

As is illustrated in Figures 10–12, the basalt groups also have distinct immobile, incompatible element ratios. For example, the LREE-enriched group has lower Ta/Nd, Sm/Nd, Y/Nb and Zr/Nb, but higher Ta/Yb, Th/Yb, Sm/Yb, Gd/Yb and La/Nb than the LREE-depleted group. These ratios are unlikely to have been significantly affected by low-temperature or hydrothermal alteration.

MAGMA EVOLUTION AND GENESIS

Variations in the major- and trace-element geochemistry, taken together with the observed phenocryst phases in these rocks, can help constrain the differentiation history of the Alboran volcanic rocks. The decrease in Al_2O_3, Sr, and CaO with increasing SiO_2 and degree of differentiation, as well as the negative Eu anomaly present in most samples (especially the most evolved: dacites and rhyolites), indicate fractionation of plagioclase, which was the major phenocrystic phase found in all rock types. The presence of clinopyroxene in the basalts through andesites, and the decreases in CaO/Al_2O_3, CaO, and Cr are consistent with clinopyroxene fractionation, whereas the decreases in MgO and Co most likely reflect olivine fractionation in the more mafic rocks. The decreases in FeO*, TiO_2, and V with decreasing SiO_2 and presence of titanomagnetite phenocrysts in all rock types illustrate the importance of titanomagnetite as a fractionating phase. Removal of ~5% titanomagnetite is necessary to explain the decrease in V from basalt to rhyolite. Finally, the decrease in P_2O_5 and the depletion in the MREE reflect fractionation of apatite and possibly amphibole. In summary, fractionation of plagioclase, clinopyroxene, titanomagnetite, olivine, apatite and amphibole can explain most of the observed variations in the major and compatible trace elements. Nevertheless, the presence of xenocrysts and the large range in Pb concentration in the dacites and rhyolites of 1.5 to 66 ppm (only three samples, however, have Pb > 15.5 ppm) suggest that crustal contamination was also an important process affecting the chemistry in at least the more evolved magmas.

The geochemistry of the volcanic rocks from the Alboran places important constraints on their origins. The calc-alkaline character of most of these rocks, which range from basalt through rhyolite, is a typical feature of subduction zone volcanism. Furthermore, andesites and dacites occur almost exclusively in island arcs or along active continental margins. The trace-element systematics provide further strong support for a subduction origin of the Alboran volcanic rocks. These include (1) the spiked incompatible-element patterns, (2) troughs at Nb, Ta, and Ti on incompatible-element diagrams (Fig. 9A), (3) high Ba/La, Ba/(Nb, Ta), K/(Nb, Ta) ratios, and (4) low (Nb, Ta)/REE, Nb/U, and Ce/Pb ratios. Because of the high solubility of mobile elements (e.g., Rb, Ba, U, K, Sr, Pb) in hydrous fluids at mantle temperatures, these elements are transported from the slab to the overlying asthenospheric wedge, resulting in enrichment of the wedge (and the melts derived from the wedge) in these elements (e.g., Gill, 1981). Melts of sediments can also enrich the wedge in these elements. Such enrichment processes can explain the spikes in the mobile elements on multi-element diagrams (e.g., see the LREE-depleted basalts in Fig. 9A), as well as high ratios in most samples of mobile elements to immobile elements, such as Nb and Ta. The troughs on the incompatible-element diagrams at Nb and Ta can reflect the low abundances of these elements in sediments and/or the retention of these elements in the source by a residual phase such as titanite, rutile, or possibly phlogopite (e.g., Gill, 1981; Wilson, 1989; Ionov and Hofmann, 1995).

Although contamination or mixing of MORB melts with continental crustal material can generate similar incompatible-element characteristics (e.g., Wilson, 1989) to those observed in some of the basaltic samples, crustal assimilation (during ascent) cannot alone explain the incompatible-element chemistry of the Alboran volcanic rocks. For example, the enriched basaltic samples extend to higher compositions of many elements (e.g., K_2O, Ba, Sr, Pb, Th, U, LREEs) than generally found in MORB or the continental crust (Hofmann, 1988; Taylor and McLennan, 1985). Furthermore, crustal assimilation during fractional crystallization (AFC) cannot explain the inverse correlations of SiO_2 with Nb/Zr and Nd/Sm in the basaltic samples, because with increasing differentiation (as reflected by increasing SiO_2), both ratios should increase, not decrease. The variation in Ta/Nd and Sm/Nd ratios in the basaltic samples are also inconsistent with crustal contamination (Fig. 10). The extreme depletion in highly incompatible, immobile elements observed in some of the LREE-depleted basalts are primarily found in subduction environments and are believed to form by high degrees of melting in the presence of water and/or as a result of progressive depletion of the source (e.g., Stolper and Newman, 1994). Finally, we note the striking similarity between the incompatible-element abundances of the LREE-enriched Alboran basaltic rocks and those from basaltic rocks in the active Aeolian Arc, also in the western Mediterranean (Fig. 9A). We conclude that the major- and trace-element compositions of the volcanic rocks provide evidence that subduction was active in the Alboran from 6 to at least 12 Ma.

The incompatible-element data for the Alboran basaltic rocks can also be used to constrain the residual mineralogy of the sources of both groups. The LREE-depleted basalts have heavy (H)REE patterns with near zero to slightly positive slopes and $(Sm/Yb)_N$, $(Gd/Yb)_N$, and $(Dy/Yb)_N \leq 1$ (Fig. 9A), indicating that garnet was not a residual phase. The enrichment or peaks in mobile elements (Rb, U, K, Pb, and Sr) vs. the depletion or troughs in immobile elements (Th, HFSE, and REE) could reflect high degrees of melting of sources metasomatized by hydrous fluids from the subducting slab (e.g., Stolper and Newman, 1994). A high degree of melting (because of high water content) will result in an apparent depletion (i.e., dilution) in immobile elements, which are not enriched by the hydrous fluids. The mobile elements are, however, continually enriched in the wedge by new fluid fluxes. In conclusion, these basalts are consistent with derivation from metasomatized MORB-type material in the mantle wedge above a subducting slab.

The steep negative slopes of the HREE patterns and $(Sm/Yb)_N$, $(Gd/Yb)_N$, and $(Dy/Yb)_N > 1$ (Fig. 9A) indicate that garnet may have been a residual phase during melting to form the LREE-enriched basalts. Although garnet is only stable at depths >75–80 km (pressures in excess of 2.3–2.5 GPa) in peridotite, it can be stable to depths as shallow as 40 km in pyroxenite (Hirschmann and Stolper, 1996). The negative anomalies on incompatible-element diagrams in Rb, Ba, K, Zr, Ti (and possibly Nb and Ta) and the lack of a pronounced Pb anomaly (in contrast to the LREE-depleted basalts; see Fig. 9A) most likely reflect the presence of residual phlogopite (± amphibole) in the source, which can be enriched in all of these elements (Ionov and Hofmann, 1995, and references therein). The LREE-enriched basalt, therefore, could have been derived from a phlogopite-bearing garnet-pyroxenite or -peridotite source within the mantle wedge above the subducting slab.

There are two possible interpretations for enrichment in Th, LREE, and MREE in the LREE-enriched basalts. First, they could reflect derivation from an enriched OIB- or plume-type of source. Using seismic tomography and isotope geochemistry, it has been shown that large-scale upwelling of plume material has been occurring throughout the Cenozoic beneath the eastern Atlantic, western Mediterranean, and western and central Europe (Hoernle et al., 1995). The trace-element pattern for a basalt sample from Gomera (Canary Islands) with the Sr, Nd, and Pb isotopic composition of this plume end-member (LVC) is shown in Figure 9A (S. Dorn and K. Hoernle, unpubl. data). The close similarity of the incompatible-element composition of this and other samples from the aforementioned areas with those from high $^{238}U/^{204}Pb$ (HIMU)-type ocean islands, such as Saint Helena, suggest an origin of the LVC plume component from recycled oceanic crust. Recycled ocean crust is likely to be present in the mantle as garnet pyroxenite. As is commonly observed in peridotite massifs (believed to be obducted portions of the upper mantle) in northern Morocco (Beni Boussera) and southern Spain (Ronda), pyroxenite layers (with and without garnet) commonly occur within a peridotite matrix. Therefore, the OIB-type, LREE-enriched end-member is likely to occur as garnet pyroxenite layers within depleted (MORB-type) peridotite. It has been shown in regions of upwelling mantle, such as beneath the nearby Canary Islands, that zones of both OIB- and MORB-type material can occur over distances of <100 km (Hoernle et al., 1991; Hoernle and Schmincke, 1993). Subduction of ocean crust beneath the Alboran resulted in metasomatism of both MORB and OIB components within the mantle wedge by hydrous fluids, which resulted in the stabilization of phlogopite in the garnet-pyroxenite component. Both garnet and phlogopite remained in the residuum during melting to generate the LREE-enriched basalts.

Alternatively, the trace-element characteristics of the LREE-enriched basalts could reflect the presence of sediments in the source, as has also been proposed for the Aeolian Arc Volcanic Rocks with similar chemistry (Fig. 9; Ellam et al., 1989). If this is the case, then the steep HREE patterns do not necessarily require the presence of garnet in the source. The presence of phlogopite (± amphibole) in the residuum of the Alboran basalts may reflect their derivation from lithospheric mantle sources, in contrast to derivation of the Aeolian Arc Basalts from asthenospheric sources. Isotope data are crucial for placing further constraints on the source compositions for both basalt groups and for distinguishing between involvement of sediments or OIB-type material.

DISCUSSION

As indicated above, the geochemistry of Miocene (6–12 Ma) volcanic rocks from Sites 977 and 978 can best be explained in the context of subduction. Based on available geochemical data, rocks from the volcanic belt in Figure 1 have similar compositions to the samples analyzed in this study, as is illustrated by the comparison with Cabo de Gata (e.g., Toscani et al., 1990; Fernandez Soler, 1992; see also

Fig. 6). The major- and trace-element chemistry of Miocene tholeiitic, calc-alkaline, potassic and lamproitic rocks in the Alboran Region have been interpreted to reflect subduction in the region (Araña and Vegas, 1974; Bellon and Brousse, 1977; Delarue and Brousse, 1974; Foley et al., 1987; Venturelli et al., 1988; Nelson et al., 1986; Torres-Roldán et al., 1986; Venturelli et al., 1984). Therefore, the 400 km northeast-trending volcanic zone may represent a volcanic arc formed by subduction of ocean crust during the Miocene.

Additional support for northeast-trending subduction comes from the depth of earthquake epicenters and seismic tomography. The epicenters of two earthquakes in 1954 and 1973, located at 630 km and 640 km, respectively, beneath southern Spain, are interpreted to reflect the presence of a subducted slab at the base of the upper mantle (e.g., Isacks and Molnar, 1971; Chung and Kanamori, 1976; Udías et al., 1976; Grimison and Chen, 1986). The calculated east-west–trending principal stress axis (Udías et al., 1976) is consistent with northwest-dipping subduction (Blanco and Spakman, 1993; Zeck, 1996). Delay-time tomography shows that the presence of a positive *P*-wave velocity anomaly between 200 and 700 km depths resembles a cold, subducted, lithospheric slab (Blanco and Spakman, 1993). The southwest-northeast strike and ~600 km length of this anomaly are similar to that of the Miocene volcanic belt (see Fig. 1). Although oceanic lithosphere is generally not thicker than ~100 km, the 250-km thickness (and 600-km length) of the *P*-wave anomaly no doubt in part reflects thermal equilibration of the surrounding warmer mantle with the colder slab (Zeck, 1996) and the resolution of the tomographic model. Data from the new seismic network in Morocco show a similar *P*-wave anomaly beneath northeastern Morocco, the Alboran, and southeastern Spain between 150 and 350 km (Seber et al., 1996a).

Although it is difficult to constrain the onset of subduction, the oldest ages of volcanism in the Alboran region (20–25 Ma) suggest that it may have occurred near the Oligocene/Miocene boundary (Fig. 2). This boundary is associated with a major change in the plate kinematics in the North Atlantic region. Not only did movement within the Pyrenees and Biscay cease, but the European-African plate boundary shifted to the Azores-Alboran fracture zone (Roest and Srivastava, 1991). The Oligocene/Miocene boundary also coincides with the beginning of subsidence to form the Alboran Basin and exhumation of metamorphic nappe complexes in southern Spain (Comas et al., 1992; Zeck et al., 1992; Zeck, 1996). These events suggest that the Alboran Basin may have been formed by back-arc processes (Torres-Roldán et al., 1986) and that the Alboran back-arc basin (and possibly other Mediterranean back-arc basins) distinguishes itself from Pacific-style back-arc basins primarily because subduction occurs beneath continental crust under compression from continent-continent collisions.

The lower velocities above 200 km in the tomographic model of Blanco and Spakman (1993) and the lack of seismicity under the Alboran and adjacent regions of southern Spain and northern Morocco (from 2° to 8°W) between depths of 120 and 180 km (Seber et al., 1996b; Fig. 2) are consistent with the proposal that the subducted lithospheric slab is detached (Blanco and Spakman, 1993; Zeck, 1996). Warmer and lighter asthenospheric material from greater depth is likely to flow into the void formed by the detachment and sinking of a cold lithospheric slab. Decompression melting of inflowing asthenosphere could result in the formation of low-degree, alkali-basalt melts, which suggests that detachment occurred 5–6 Ma or slightly before, when the composition of volcanic rocks changed from primarily calc-alkaline to alkaline (Fig. 2).

Detachment could also explain several other phenomena that occurred at or near the Miocene/Pliocene boundary. Whereas deformation and uplift in the Alboran region moved westward at the end of the Miocene and beginning of the Pliocene, subsidence in the Alboran Basin moved to the east and southeast (i.e., toward and east of the Alboran Ridge; Docherty and Banda, 1995). Release of the downward pull from the subducting slab on the bent portion of the slab and in-flow of warmer and lighter asthenosphere into the gap above the slab could cause uplift above the sinking slab (Wortel and Spakman, 1992; Zeck et al., 1992; Blanco and Spakman, 1993). Temporary uplift of the Gibraltar arc on the western margin of the Alboran Sea 5–6 m.y. ago may in part be responsible for closing the Strait of Gibraltar, which resulted in the Messinian salinity crises in the Mediterranean. Subsidence of the eastern portion of the Alboran in the early Pliocene, however, is difficult to explain unless part of the lithospheric mantle beneath the eastern Alboran was removed or delaminated (Docherty and Banda, 1995). It is possible that during the detachment process a piece of the lithospheric mantle beneath the eastern Alboran may have been removed by the sinking slab. Finally, detachment of the lithospheric slab, or subsequent mantle upwelling, might also trigger delamination of the lithospheric mantle on the overriding plate, which could explain the gap in seismic activity, low P_n-wave velocities, and high seismic-wave attenuation at depths of 20–60 km presently beneath the Alboran Sea and Gibraltar Arc (Seber et al., 1996b).

Although northwest-dipping subduction of oceanic crust in the Miocene beneath the Alboran, followed by slab detachment and lithospheric delamination in the Pliocene, does not provide a unique solution for the geological, geophysical, tectonic, and structural data (e.g., see "Introduction" in Comas, Zahn, Klaus, et al., 1996), it shows that the available data can at least be interpreted in the context of such a model.

CONCLUSIONS

The tholeiitic to calc-alkaline basalt to rhyolite volcanic rocks from Holes 977A and 978A in the eastern central Alboran Sea range in age from 6.1 Ma to 12.1 Ma The ages conform to the stratigraphy and to ages from microfossils, where available. The major- and trace-element geochemistry shows strong affinities to volcanic rocks from subduction zones, which indicates that subduction most likely occurred beneath the eastern Alboran 6.1 to at least 12.1 Ma. The incompatible-element data also require the presence of both depleted (MORB-source) and enriched (ocean-island or sediment) components in the mantle beneath the Alboran.

ACKNOWLEDGMENTS

We acknowledge Alain Mascle and Menchu Comas for constructive reviews of this manuscript and Susanne Straub for helpful comments. Kerstin Wolff, Jan Sticklus, Tom Arpe, and Marianne Stavesand are thanked for their help with the analytical work. We thank Menchu Comas and Juan Manuel Fernandez Soler for providing us with a preliminary version of a manuscript on Alboran volcanic samples obtained by diving. We are grateful to the DFG for funding this project (Bo 912/6).

REFERENCES

Ait-Brahim, L., and Chotin, P., 1990. Oriental Moroccan neogene volcanism and strike-slip faulting. *J. Afr. Earth Sci.*, 11:273–280.

Aparicio, A., Mitjavila, J.M., Araña, V., and Villa, I.M., 1991. La edad del volcanismo de las islas Columbrete Grande y Alborán (Mediterráneo occidental). *Bol. Geol. Min.*, 102:562–570.

Araña, V., and Vegas, R., 1974. Plate tectonics and volcanism in the Gibraltar Arc. *Tectonophysics*, 24:197–212.

Bellon, H., 1976. Séries magmatique néogènes et quarternaires du pourtour de la méditerranée occidentale, comparées dans leur cadre géochronométrique: implications géodynamiques [Ph.D. dissert.]. Univ. de Paris-Sud Centre D'Orsay.

Bellon, H., Bordet, P., and Montenat, C., 1983. Chronologie du magmatisme néogène des Cordillères bètiques (Espagne méridionale). *Bull. Soc. Geol. Fr.* 7:205–217.

Bellon, H., and Brousse R., 1977. Le magmatisme périméditerranén occidental: essai de synthése. *Bull. Soc. Geol. Fr.,* 7:469–480.

Bellon, H., and Letouzey, J., 1977. Volcanism related to plate tectonics in the western and eastern Mediterranean. *In* Biju-Duval, B., and Montadert, L. (Eds.), *International Symposium on the Structural History of the Mediteranean Basins:* Paris (Ed. Technip), 165–184.

Blanco, M.J., and Spakman, W., 1993. The *P*-wave velocity structure of the mantle below the Iberian Peninsula: evidence for subducted lithosphere below southern Spain. *Tectonophysics,* 221:13–34.

Bordet, P., Esquevin, J., and de Larouzière, F.D., 1982. Sur l'âge tortonien de certains des granitoides inclus dans les conglomérat miocènes de l'Espagne du Sud-Est. *C. R. Acad. Sci. Ser. 2,* 295:483–486.

Bourdier, J.L., 1986. Formation sous-marine de brèches andésitiques au Ras Tarf (Rif, Maroc). *C. R. Acad. Sciences Ser. 2,* 303:619–622.

Boynton, W.V., 1984. Cosmochemistry of the rare earth elements: meteorite studies. *In* Henderson, P. (Ed.), *Rare Earth Element Geochemistry:* New York (Elsevier), 63–114.

Chaffey, D.J., Cliff, R.A., and Wilson, B.M., 1989. Characterization of the St. Helena magma source. *In* Saunders, A.D., and Norry, M.J. (Eds.), *Magmatism in the Ocean Basins.* Geol. Soc. Spec. Publ. London, 42:257–276.

Chung, W.-Y., and Kanamori, H., 1976. Source process and tectonic implications of the Spanish deep-focus earthquake of March 29, 1954. *Phys. Earth Planet. Inter.,* 13:85–96.

Comas, M.C., García-Dueñas, V., and Jurado, M.J., 1992. Neogene tectonic evolution of the Alboran Basin from MCS data. *Geo-Mar. Lett.,* 12:157–164.

Comas, M.C., Zahn, R., Klaus, A., et al., 1996. *Proc. ODP, Init. Repts.,* 161: College Station, TX (Ocean Drilling Program).

Dalrymple, G.B., and Duffield, W.A., 1988. High precision $^{40}Ar/^{39}Ar$ dating of Oligocene tephra from the Mogollon-Datil volcanic field using a continuous laser system. *Geophys. Res. Lett.,* 15:463–466.

DeJong, K., 1993. The tectono-metamorphic and chronologic development of the Betic Zone (SE Spain) with implications for the geodynamic evolution of the western Mediterranean area. *Verh. Kon. Ned. Akad. Wetensch.,* 96:295–333.

Delarue, C., and Brousse, R., 1974. Volcanisme miocène en subduction au Maroc à l´extrémité orientale de l´arc de Gibraltar. *C. R. Acad. Sci.,* 279:971–974.

Dercourt, J., Zonenshain, L.P., Ricou, L.E., Kazmin, V.G., Le Pichon, X., Knipper, A.L., Grandjacquet, C., Sbortshikov, I.M., Geyssant, J., Lepvrier, C., Pechersky, D.H., Boulin, J., Sibuet, J.C., Savostin, L.A., Sorokhtin, O., Westphal, M., Bazhenov, M.L., Lauer, J.P., and Bijou-Duval, B., 1986. Geological evolution of the Tethys belt from the Atlantic to the Pamirs since the Lias. *Tectonophysics,* 123:241–315.

Dewey, J.F., Helman, M.L., Turco, E., Hutton, D.H.W., and Knott, S.D., 1989. Kinematics of the western Mediterranean. *In* Coward, M.P., Dietrich, D., and Park, R.G. (Eds.), *Conference on Alpine Tectonics.* Geol. Soc. Spec. Publ. London, 45:265–283.

Di Battistini, G., Toscani, L., Iaccarino, S., and Villa, I.M., 1987. K/Ar ages and the geological setting of calc-alkaline volcanic rocks from Sierra de Gata, SE Spain. *Neues Jahrb. Mineral.,* 8:369–383.

Docherty, C., and Banda, E., 1995. Evidence for the eastward migration of the Alboran Sea based on regional subsidence analysis: a case for basin formation by delamination of the subcrustal lithosphere? *Tectonics,* 14:804–818.

Duffield, W.A., and Dalrymple, G.B., 1990. The Taylor Creek Rhyolite of New Mexico: a rapidly emplaced field of lava domes and flows. *Bull. Volcanol.,* 52:475–487.

Dupuy, C., Dostal, J., and Boivin, P.A., 1986. Geochemistry of ultramafic xenoliths and their host alkali basalts from Tallante, southern Spain. *Mineral. Mag.,* 50:231–239.

Ellam, R.M., Hawkesworth, C.J., Menzies, M.A., and Rogers, N.W., 1989. The volcanism of southern Italy: role of subduction and the relationship between potassic and sodic alkaline magmatism. *J. Geophys. Res.,* 94:4589–4601.

Fernandez Soler, J.M.F., 1992. El volcanismo calco-alcalino de Cabo de Gata (Almeria) [Ph.D. dissert.]. *Est. Vulcanol. Petrol., Univ. de Granada.*

Foley, S.F., Venturelli, G., Green, D.H., and Toscani, L., 1987. The ultrapotassic rocks: characteristics, classifications, and constraints for petrographic models. *Earth Sci. Rev.,* 24:81–134.

Garbe-Schoenberg, C.-D., 1993. Simultaneous determination of thirty-seven trace elements in twenty-eight international rock standards by ICP-MS. *Geostand. Newsl.,*17:81–97.

García-Dueñas, V., Balanyá, J.C., and Martínez-Martínez, J.M., 1992. Miocene extensional detachments in the outcropping basement of the northern Alboran basin (Betics) and their tectonic implications. *Geo-Mar. Lett.,* 12:88–95.

Giermann, G., Pfannenstiel, M., and Wimmenauer, W., 1968. Relation entre morphologie, tectonique et volcanisme en mer d'Alboran (Mediterranée occidentale): resultats preliminaires de la campagne Jean-Charcot (1967). *C. R. Somm. Seances Soc. Geol. Fr.,* 4:116–118.

Gill, J.B., 1981. *Orogenic Andesites and Plate Tectonics:* New York (Springer-Verlag).

Grimison, N.L., and Chen, W.-P., 1986. The Azores-Gibraltar plate boundary: focal mechanisms, depths of earthquakes, and their tectonic implications. *J. Geophys. Res.,* 91:2029–2047.

Harland, W.B., Cox, A.V., Llewellyn, P.G., Pickton, C.A.G., Smith, A.G., and Walters, R., 1982. *A Geologic Time Scale:* Cambridge (Cambridge Univ. Press).

Hernandez, J., and Bellon, H., 1985. Chronologie K-Ar du volcanisme miocéne. *Rev. Geol. Geogr. Phys.,* 26:85–94.

Hernandez, J., de Larouzière, F.D., Bolze, J., and Bordet, P., 1987. Le magmatisme néogène bético-rifain et le couloir de décrochement trans-Alboran. *Bull. Soc. Geol. Fr.,* 3:257–267.

Hirschmann, M.M., and Stolper, E.M., 1996. A possible role for garnet pyroxenite in the origin of the "garnet signature" in MORB. *Contrib. Mineral. Petrol.,* 124:185–208.

Hoernle, K., and Schmincke, H.-U., 1993. The role of partial melting in the 15-Ma geochemical evolution of Gran Canaria: a blob model for the Canary Hotspot. *J. Petrol.,* 34:599–627.

Hoernle, K.A., Tilton, G., and Schmincke, H.-U., 1991. The Sr-Nd-Pb isotopic evolution of Gran Canaria: evidence for shallow enriched mantle beneath the Canary Islands. *Earth Planet. Sci. Lett.,* 106:44–63.

Hoernle, K., Werner, R., Geldmacher, J., Wienecke, M., Hauff, F., Cruz, V., Duggen, S., Zankl, G., Aarburg, S., Neu, B., 1997. *Cruise Summary Report POS235:* Kiel (Institute für Meereskunde), 17.

Hoernle, K., Zhang, Y.S., and Graham, D., 1995. Seismic and geochemical evidence for large-scale mantle upwelling beneath the eastern Atlantic and western central Europe. *Nature,* 374:34–39.

Hofmann, A.W., 1988. Chemical differentiation of the Earth: the relationship between mantle, continental crust and oceanic crust. *Earth Planet. Sci. Lett.,* 90:297–314.

Horvath, F., and Berckhemer, H., 1982. Mediterranean back arc basins. *In* Berckhemer, H., and Hsü, K.J. (Eds.), *Alpine-Mediterranean Geodynamics.* Ber. Inst. Meteorol. Geophys. Univ. Frankfurt/Main, Geodyn. Ser., 7:141–173.

Ionov, D.A., and Hofmann, A.W., 1995. Nb-Ta-rich mantle amphiboles and micas: implications for subduction related metasomatic trace element fractionations. *Earth Planet. Sci. Lett.,* 131:341–356.

Isacks, B., and Molnar, P., 1971. Distribution of stresses in the descending lithosphere from a global survey of focal-mechanism solutions of mantle earthquakes. *Rev. Geophys. Space Phys.,* 9:103–174.

Kastens, K.A., 1992. Did glacio-eustatic sea level drop trigger the Messinian salinity crisis? New evidence from Ocean Drilling Program Site 654 in the Tyrrhenian Sea. *Paleoceanography,* 7:333–356.

Le Maitre, R.W., Bateman, P., Dudek, A., Keller, J., Lameyre Le Bas, M.J., Sabine, P.A., Schmid, R., Sorensen, H., Streckeisen, A., Woolley, A.R., and Zanettin, B., 1989. *Classification of Igneous Rocks and Glossary of Terms:* Oxford (Blackwell).

Le Pichon, X.G., Pautot, G., and Weill, J.P., 1972. Opening of the Alboran sea. *Nature,* 236:83–85.

Loomis, T.P., 1975. Tertiary mantle diaprism, orogeny and plate tectonics east of the Strait of Gibraltar. *Am. J. Sci.,* 275:1–30.

Morley, C.K., 1992. Notes on Neogene basin history of the western Alboran Sea and its implication for the tectonic evolution of the Rif-Betics orogenic belts. *J. African Earth Sci.,* 14:57–65.

————, 1993. Discussion of origins of hinterland basins to the Rif-Betic Cordillera and Carpathians. *Tectonophysics,* 226:359–376.

Munksgaard, N.C., 1984. High $\delta^{18}O$ and possible pre-eruptional Rb-Sr isochrons in cordierite-bearing Neogene volcanics from SE-Spain. *Contrib. Mineral. Petrol.,* 87:351–358.

Nelson, D.R., McCulloch, M.T., and Sun, S.-S., 1986. The origins of ultrapotassic rocks as inferred from Sr, Nd and Pb isotopes. *Geochim. Cosmochim. Acta.*, 50:231–245.

Nobel, F.A., Andriessen, P.A.M., Hebeda, E.H., Priem, H.N.A., and Rondeel, H.E., 1981. Isotopic dating of the post-alpine neogene volcanism in the Betic Cordilleras, Southern Spain. *Geol. Mijnbouw*, 60:209–214.

Pearce, J.A., 1983. The role of sub-continental lithosphere in magma genesis at active continental margins. *In* Hawkesworth, C.J., and Norry, M.J. (Eds.), *Continental Basalts and Mantle Xenoliths:* Nantwich (Shiva Publ.), 230–249.

Platt, J.P., and Vissers, R.L.M., 1989. Extensional collapse of thickened continental lithosphere: a working hypothesis for the Alboran Sea and Gibraltar Arc. *Geology*, 17:540–543.

Rickwood, P.C., 1989. Boundary lines within petrological diagrams which use oxides of major and minor elements. *Lithos*, 22:247–263.

Roest, W.R., and Srivastava, S.P., 1991. Kinematics of the plate boundaries between Eurasia, Iberia and Africa in the North Atlantic from the late Cretaceous to present. *Geology*, 19:613–616.

Royden, L.H., 1993. Evolution of retreating subduction boundaries formed during continental collision. *Tectonics*, 12:629–638.

Seber, D., Barazangi, M., Ibenbrahim, A., and Demnati, A., 1996a. Geophysical evidence for lithospheric delamination beneath the Alboran Sea and Rif-Betic mountains. *Nature*, 379:785–790.

Seber, D., Barazangi, M., Tadili, B.A., Ramdani, M., Ibenbrahim, A., and Sari, D.B., 1996b. Three-dimensional upper mantle structure beneath the intraplate Atlas and interplate Rif mountains of Morocco. *J. Geophys. Res.*, 101:3125–3138.

Stolper, E., and Newman, S., 1994. The role of water in the petrogenesis of Mariana trough magmas. *Earth Planet. Sci. Lett.*, 121:293–325.

Taylor, S.R., and McLennan, S.M., 1985. *The Continental Crust: Its Composition and Evolution:* Oxford (Blackwell Scientific).

Torres-Roldán, R.L., Poli, G., and Peccerillo, A., 1986. An early Miocene arc–tholeiitic magmatic dike event from the Alboran-Sea: evidence for precollisional subduction and back-arc crustal extension in the westernmost Mediterranean. *Geol. Rundsch.*, 75:219–234.

Toscani, L., Venturelli, G., Barbieri, M., Capedri, S., Fernandez Soler, J.M., and Oddone, M., 1990. Geochemistry and petrognenesis of two-pyroxene andesites from Sierra de Gata (SE Spain). *Mineral. Petrol.*, 41:199–213.

Udías, A., López Arroyo, A., and Mezcua, J., 1976. Seismotectonic of the Azores-Alboran region. *Tectonophysics*, 31:259–289.

van den Bogaard, P., 1995. $^{40}Ar/^{39}Ar$ ages of sanidine phenocrysts from Laacher See tephra (12.900 yr BP): chronostratigraphic and petrological significance. *Earth Planet. Sci. Lett.*, 133:163–174.

Venturelli, G., Capedri, S., Di Battistini, G., Crawford, A., Kogarko, L.N., and Celestini, S., 1984. The ultrapotassic rocks from southeastern Spain. *Lithos*, 17:37–54.

Venturelli, G., Salvioli-Mariani, E., Foley, S.F., Capedri, S., and Crawford, A.J., 1988. Petrogenesis and conditions of crystallization of Spanish lamproitic rocks. *Can. Mineral.*, 26:67–79.

Vissers, R.L.M., Platt, J.P., and van der Wal, D., 1995. Late orogenic extension of the Betic Cordillera and the Alboran Domain: a lithospheric view. *Tectonics*, 14:786–803.

Weijermars, R., 1985. Uplift and subsidence history of the Alboran Basin and a profile of the Alboran Diapir (W-Mediterranean). *Geol. Mijnbouw*, 64:349–356.

Wilson, M., 1989. *Igneous Petrogenesis: A Global Tectonic Approach:* London (Unwin Hyman).

Wortel, M.J.R., and Spakman, W., 1992. Structure and dynamics of subducted lithosphere in the Mediterranean region. *Proc. K. Ned. Akad. Wet.*, 95:325–347.

Zeck, H.P., 1996. Betic-Rif orogeny: subduction of Mesozoic Tethys lithosphere under eastward drifting Iberia, slab detachment shortly before 22 Ma, and subsequent uplift and extensional tectonics. *Tectonophysics*, 254:1–16.

Zeck, H.P., Monié, P., Villa, I.M., and Hansen, B.T., 1992. Very high rates of cooling and uplift in the Alpine belt of the Betic Cordilleras, southern Spain. *Geology*, 20:79–82.

Date of initial receipt: 12 May 1997
Date of acceptance: 2 December 1997
Ms 161SR-264